

UNCLASSIFIED

AD NUMBER

AD912099

LIMITATION CHANGES

TO:

Approved for public release; distribution is unlimited.

FROM:

Distribution authorized to U.S. Gov't. agencies only; Test and Evaluation; 18 APR 1973. Other requests shall be referred to Air Force Cambridge Research Labs., Attn: LZ, L. G. Hanscom Field, Bedford, MA 01730.

AUTHORITY

AFCRL ltr dtd 21 Jan 1974

THIS PAGE IS UNCLASSIFIED

14  
AFCRL-TR-73-0317 ✓  
16 MAY 1973 ✓  
PHYSICAL SCIENCES RESEARCH PAPERS, NO. 549



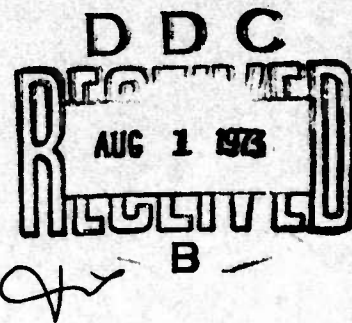
**AIR FORCE CAMBRIDGE RESEARCH LABORATORIES**  
L. G. HANSCOM FIELD, BEDFORD, MASSACHUSETTS

AD 912099

**Trailblazer II Rocket Tests on the Reentry  
Plasma Sheath: Vehicle Performance and  
Plasma Predictions (Flights No. 1 - 3)**

JOHN F. LENNON

AD No. \_\_\_\_\_  
DDC FILE COPY



Distribution limited to U.S. Government agencies  
only; Test and Evaluation; 18 April 1973. Other  
requests for this document must be referred to  
AFCRL, LZ, L.G. Hanscom Field, Bedford,  
Massachusetts 01730

**AIR FORCE SYSTEMS COMMAND**  
United States Air Force



14  
AFCRL-TR-73-0317

16 MAY 1973

9 PHYSICAL SCIENCES RESEARCH PAPERS, NO. 549

AFCRL-PSRP-549



MICROWAVE PHYSICS LABORATORY PROJECT 4642

**AIR FORCE CAMBRIDGE RESEARCH LABORATORIES**

L. G. HANSCOM FIELD, BEDFORD, MASSACHUSETTS

6  
**Trailblazer II Rocket Tests on the Reentry  
Plasma Sheath: Vehicle Performance and  
Plasma Predictions (Flights No. 1 - 3).**

10 JOHN F. LENNON

11 16 May 73

12 Slope

16 AF-4642

17 4642 D2

Distribution limited to U.S. Government agencies  
only; Test and Evaluation; 18 April 1973. Other  
requests for this document must be referred to  
AFCRL, LZ, L.G. Hanscom Field, Bedford,  
Massachusetts 01730

**AIR FORCE SYSTEMS COMMAND**  
**United States Air Force**



11 800 ✓

## Abstract

The properties of the reentry plasma sheath are being studied by AFCRl. in a series of Trailblazer II rocket flights. This program is divided into two phases. The first phase has been concerned with the structure of the ionized layer that forms around the test vehicles during reentry and in particular its effect on electromagnetic signals, while the second phase is concerned with enhancing microwave transmitter performance under such conditions by introducing chemicals into the flow to reduce the free electron concentrations.

This report surveys some aspects of the first phase which consisted of three flights. The first part of the report describes the flight performance of the vehicles including trajectory, velocity history, aerodynamic heating, spin-and-precession, and overall orientation of each payload during its reentry, while the second part presents the theoretical description of the high temperature shock layer for the various flight conditions. Since the purpose of the calculations was to obtain predictions of experimental performance, a number of different models were used. The resulting flow properties are presented in some detail; in particular, the various electron density distributions are shown both in the nose region and around the vehicle. These results are analyzed and then compared with the extensive experimental data.

On the conical afterbody where three-dimensional effects due to vehicle angle of attack become important, the observed conditions could not be completely represented by the theoretical models—all of which assumed the flow to be axisymmetric. The general conclusion, however, is that the theoretical properties satisfactorily predict the actual test performance for a wide range of situations.

## Contents

1.	INTRODUCTION	1
2.	DESCRIPTION OF VEHICLE AND FLIGHT TESTS	2
3.	FLIGHT RECORD FROM GROUND RADAR	6
	3.1 Radar Trajectory	6
	3.2 Vehicle-Ground Orientation	12
	3.3 Spin	13
	3.4 Precession and Angle of Attack	14
	3.5 Transmission Angles	20
4.	HEAT TRANSFER AND TURBULENCE	22
	4.1 Transition To Turbulence	22
	4.2 Heat Transfer	23
5.	FLOW FIELD STUDIES	24
	5.1 General Background	24
	5.2 Stagnation Region	26
	5.3 Expansion Region	44
6.	SUMMARY AND CONCLUSIONS	70
	ACKNOWLEDGMENTS	71
	REFERENCES	73

## Illustrations

1. General Features of a Typical Trailblazer II Trajectory	3
2. Typical Nose Cone Configuration and Dimensions	4
3. Head-on View of the Three Flight Nose Cones Showing the Instrumentation Locations	6
4. Time History of the Reentry Velocity for the Three Flights	7
5. Variation of Velocity With Altitude for the Three Flights	7
6. Theoretical and Experimental Vehicle Deceleration	8
7. Altitude Variation With Time-from-Launch for the Three Flights	9
8. Geographical Orientation of the Three Vehicles to the Ground Stations During Descent	13
9. Frequency of Cyclic Variations in the Test Data for Each Flight	15
10. Theoretical Decay of Angle of Attack With Altitude (Allen)	17
11. Predicted Decay of Angle of Attack for the Three Sets of Flight Conditions (Leon)	19
12. Precession Frequency Variation With Altitude for the Three Flights	19
13. Typical Orientation of Transmission Vectors for the Three Flights	20
14. Typical Stagnation Point Heating Properties	24
15. Stagnation Region Electron Density: Merged Viscid-Inviscid Model	28
16. Theoretical and Flight Values for Received Signal Intensity From a Stagnation Region Antenna	29
17. Stagnation Region Electron Density (Vibrational Equilibrium Viscous Model)	30
18. Stagnation Region Electron Density (Vibrational Nonequilibrium Viscous Model)	30
19. Collision Frequency Profiles in the Stagnation Region	31
20. Effect of Freestream Velocity on Electron Density for the Two Viscous Models	31
21. Altitude Variation of Stagnation Region Electron Densities for the Two Viscous Models	33
22. Viscous Stagnation Region Vibrational Nonequilibrium Temperature Distributions	34
23. Stagnation Region Atomic Species Concentrations and Electron Production Rates	34
24. Freestream Velocity as an Altitude Scaling Factor	36
25. A Two Altitude Comparison of the Completely Viscous and the Merged Viscid-Inviscid Models	38
26. Received Signal Intensity From the Second Flight Nosecap Antenna	39

## Illustrations

27.	Power Reflection Coefficient for the Second Flight Nosecap Antenna	40
28.	Stagnation Region Electrostatic Probe Results From the Third Flight	43
29.	Flow Properties Around the Vehicle: altitude 220 kft, $V_{\infty} = 17,500$ fps	46
30.	Flow Properties Around the Vehicle: altitude 240 kft, $V_{\infty} = 17,500$ fps	46
31.	Flow Properties Around the Vehicle: altitude 240 kft, $V_{\infty} = 16,500$ fps	47
32.	Flow Properties Around the Vehicle: altitude 270 kft, $V_{\infty} = 17,500$ fps	47
33.	Variation of Peak Electron Density Around the Vehicle	49
34.	Electron Density Profiles at $S/R_N = 1.8$	49
35.	Flow Property Distributions at $S/R_N = 1.8$ : altitude 220 kft, $V_{\infty} = 17,500$ fps	50
36.	Flow Property Distributions at $S/R_N = 1.8$ : altitude 240 kft, $V_{\infty} = 17,500$ fps	50
37.	Flow Property Distributions at $S/R_N = 1.8$ : altitude 240 kft, $V_{\infty} = 16,500$ fps	50
38.	Flow Property Distributions at $S/R_N = 1.8$ : altitude 270 kft, $V_{\infty} = 17,500$ fps	50
39.	Electron Density Profiles Around the Vehicle: altitude 220 kft, $V_{\infty} = 17,500$ fps	52
40.	Electron Density Profiles Around the Vehicle: altitude 240 kft, $V_{\infty} = 17,500$ fps	
41.	Electron Density Profiles Around the Vehicle: altitude 240 kft, $V_{\infty} = 16,500$ fps	52
42.	Electron Density Profiles Around the Vehicle: altitude 270 kft, $V_{\infty} = 17,500$ fps	52
43.	Collision Frequency Profiles Around the Vehicle: altitude 220 kft, $V_{\infty} = 17,500$ fps	53
44.	Collision Frequency Profiles Around the Vehicle: altitude 240 kft, $V_{\infty} = 17,500$ fps	53
45.	Collision Frequency Profiles Around the Vehicle: altitude 240 kft, $V_{\infty} = 16,500$ fps	53
46.	Collision Frequency Profiles Around the Vehicle: altitude 270 kft, $V_{\infty} = 17,500$ fps	53
47.	Temperature Profiles Around the Vehicle: altitude 220 kft, $V_{\infty} = 17,500$ fps	54
48.	Temperature Profiles Around the Vehicle: altitude 240 kft, $V_{\infty} = 17,500$ fps	54
49.	Temperature Profiles Around the Vehicle: altitude 240 kft, $V_{\infty} = 16,500$ fps	54

## Illustrations

50. Temperature Profiles Around the Vehicle: altitude 270 kft, $V_{\infty} = 17,500$ fps	54
51. Density Profiles Around the Vehicle: altitude 220 kft, $V_{\infty} = 17,500$ fps	55
52. Density Profiles Around the Vehicle: altitude 240 kft, $V_{\infty} = 17,500$ fps	55
53. Density Profiles Around the Vehicle: altitude 240 kft, $V_{\infty} = 16,500$ fps	56
54. Density Profiles Around the Vehicle: altitude 270 kft, $V_{\infty} = 17,500$ fps	56
55. Variation of Electron Density Profiles With Freestream Velocity	57
56. Comparison of the Altitude Variation of the Stagnation and Shoulder Region Electron Density Profile	57
57. Effect of Velocity on Shock and Boundary Layer Thicknesses	58
58. Stagnation Streamline Equilibrium Electron Density	60
59. Effect of Velocity on Electron Density Profiles at $S/R_N = 1.8$	60
60. Shoulder Electron Density Profiles for Various Altitudes	61
61. Nonequilibrium Electron Density Profiles at the Shoulder	62
62. Electrostatic Probe Electron Density (Windward Position: $S/R_N = 0.3$ )	64
63. Variable Bias Electrostatic Probe Profiles (Windward: $S/R_N = 0.3$ ; Leeward: $S/R_N = 0.65$ )	64
64. Electrostatic Probe Electron Density (Windward Position: $S/R_N = 2.4$ )	65
65. Distribution of Electron Density Around the Vehicle Based on Electrostatic Probe Results	65
66. Signal Attenuation for the Third Flight Shoulder Antenna	68
67. Power Reflection Coefficient for the Third Flight Shoulder Antenna	69

## Tables

1. Vehicle and Flight Parameters for the Three Flights	5
2. Altitude-Time-Velocity History for the Three Flights (Based on Radar Data)	10
3. Radar Data for the Three Flights at Typical Altitudes	11
4. Transmission Angle Values for the Three Flights	21
5. Parametric Variation in Electrical Properties of Plasma Layers at the Stagnation Point	42



## Tables

6.	Description of the Selected Low Altitude Conditions	61
7.	S-Band Shoulder Antenna Transmission Properties	68

## Symbols

A	Reference area	V	Flight velocity
$C_D$	Drag coefficient	Vol	Volume
$C_{L\alpha}$	Slope of lift coefficient with angle of attack	$W/C_D A$	Vehicle weight-to-drag ratio
H	Total enthalpy	$c_p$	Specific heat at constant pressure
$I_A$	Roll moment of inertia	$d_E$	Effective slab thickness
$I_T$	Pitch moment of inertia	g	Acceleration of gravity
$J_0$	Zero order Bessel function of the first kind	h	Local enthalpy
K, $K_i$ , $K_r$	Dielectric constant; Imaginary component; Real component.	k	Wave number
[N]	Atomic nitrogen concentration	$k_1$	Dynamic stability parameter
[O]	Atomic oxygen concentration	$k_2$	Static stability parameter
P	Pressure	$k_3$	Spin parameter
R	Radius, power reflection coefficient	m	Mass
$R_{12}$	Power reflection coefficient (uniform, semi-infinite plasma)	n	Charged particle density
Re	Reynold's number	q	Heat, Electron charge
S	Wetted length	t	Time
SL	Signal loss	y	Distance normal to vehicle surface, Altitude
T	Temperature	$\alpha$	Attenuation constant, Angle of attack, Angle of a vehicle axis with ground station
U	Flow velocity	$\beta$	Phase constant, Altitude parameter
		$\Delta$	Unit change, Detachment distance
		x	

$\delta^*$	Boundary layer displacement thickness	<u>Subscripts</u>	
$\delta_{12}$	Relative phase difference	A	Attenuation
$\epsilon$	Angle between velocity vector and ground plane	ALT	Altitude component
$\Theta$	Transmission angle, Allen's symbol for $\epsilon$	B	Base of vehicle
$\nu$	Collision frequency	E	Initial reentry conditions
$\rho$	Density	EQ	Vibrational equilibrium
$\sigma$	Conductivity	e	Electron, Boundary layer edge
$\phi$	Precession rate	i, j	Indexing parameters
$\psi$	Location factor	MAX	Maximum
$\omega$	Spin frequency	N	Nose of vehicle
		NEQ	Vibrational nonequilibrium
		o	Reference condition
		R	Reflection
		ST	Stagnation condition
		T	Total
		W	Wall
		$\infty$	Freestream condition
<u>Superscript</u>			
.	$\frac{d}{dt}$		

# **Trailblazer II Rocket Tests on the Reentry Plasma Sheath: Vehicle Performance and Plasma Predictions (Flights No. 1—3)**

## **1. INTRODUCTION**

The data and analyses contained in this report are from Trailblazer II vehicles launched by AFCRL in a continuing series of experiments (Poirier et al, 1969; Hayes, 1972, Rotman, 1972; and Hayes et al, 1972). This program is divided into two phases. The first phase consisted of the first three flights—which are described in this report—and was devoted to the study of the effects of the plasma sheath on microwave systems. This involved signal transmission from various positions on the nose cone to examine effects of the plasma as a whole; the use of numerous types of diagnostic sensors for measuring the local properties; and the evaluation of the various theoretical models of the reentry flow field based on their ability to predict the observed results. The second phase of the program is concerned with the actual modification of the plasma in order to eliminate various effects on test vehicle transmission. This aspect of the program began with the fourth flight which contained not only transmitting and sensing devices, but also an injection system at the vehicle shoulder. This system introduced a chemical alleviant into the flow over a side antenna in order to reduce the electron density. This approach altered only the plasma passing directly over the antenna. On the fifth flight, which will take place this year, the payload will be equipped with a Teflon covered nose cap and the electrophilic

(Received for publication 15 May 1973)

ablation products emitted by this coating during reentry spread around the whole surface. Thus, two different methods of enhancing antenna transmission will have been observed under similar flight conditions. Another feature will be a high power experiment concerned with breakdown in the presence of a plasma. The final flight will continue the high power testing and will include an evaluation of the performance of a chemical alleviant different from that tested on the fourth flight of the series.

The Trailblazer II experiments in the AFCRL series have all employed the same launch system, and the flight performances have been similar. Dimensions of all the nose cones were identical, and the antenna test systems and diagnostic probes included on the various flights were designed to provide overlapping measurements of the test environment.

To summarize, this report presents the flight performance data for the first three launches, analyzes the aerodynamic behavior of the vehicles as related to the experiments, and discusses the prediction of reentry flow properties based on various theoretical models.

## 2. DESCRIPTION OF VEHICLE AND FLIGHT TESTS

The reentry nose cones are each launched on a Trailblazer II vehicle, which is a four-stage solid-propellant rocket. After the first two stages drive the vehicle to an altitude of about 200 miles, the last two stages propel the reentry nose back toward the atmosphere in an almost vertical trajectory.

During the ascending part of the flight, the vehicle is fin-stabilized. Shortly after launch, the canted second-stage fins induce spinning and as the vehicle leaves the atmosphere, its spin rate is high enough to ensure that it will be spin-stabilized throughout the remainder of the flight.

The last two stages are enclosed in a structural shell (velocity package) as shown in Figure 1 and face rearward during the launch. At about 250 kft, the velocity package separates from the spent second-stage motor and coasts to apogee. As the velocity package begins its descent, the X-248 third-stage motor fires, propelling the reentry nose cone out of the velocity package. The 15-in. fourth-stage spherical motor provides the final thrust necessary to boost the nose cone velocity to about 17,000 fps by the time the nose cone begins reentry.

The reentry nose cone as depicted in Figure 2 is a  $9^\circ$  hemisphere-cone fabricated entirely of aluminum. Its dimensions are: nose cap radius, 6.333 in.; total length, 26.47 in.; base diameter, 19.17 in. The instrumented nose cone weighs about 70 lb, including the spent fourth-stage motor which remains within the reentry body. So that the measured plasma properties can be compared with the values predicted from flow-field calculations, the heat-sink method of thermal

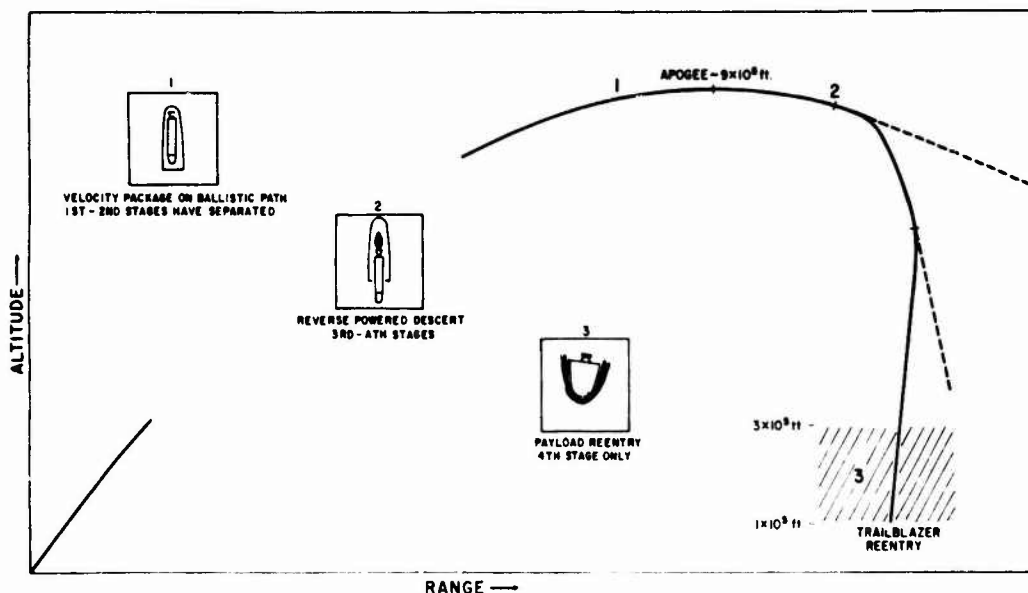
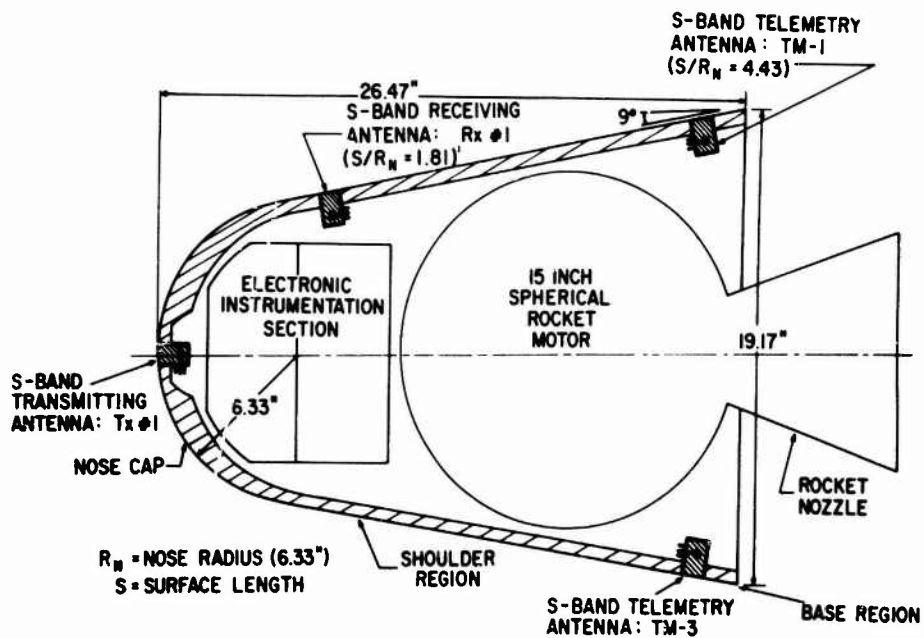


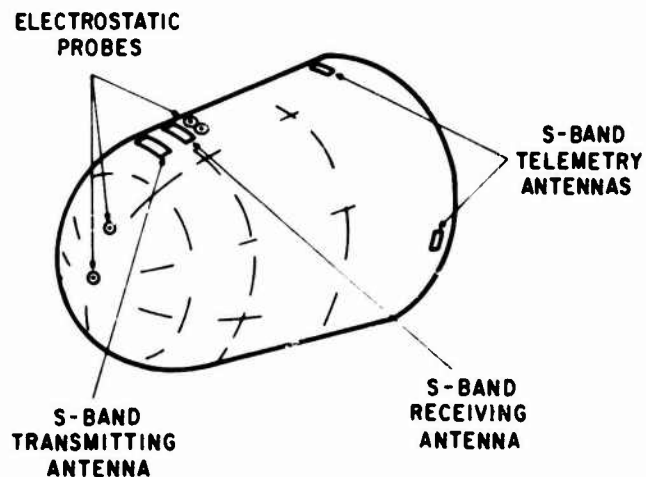
Figure 1. General Features of a Typical Trailblazer II Trajectory

protection (no ablative coatings) is used to ensure that the flow about the vehicle is not contaminated with ablation products. The aluminum nose provided sufficient protection to ensure survival to around 100 kft.

The three flight packages contained a variety of antennas and diagnostic probes, and their locations on the different flights can be seen in Figure 3 and Table 1. This table contains a breakdown of the various vehicle and flight parameters for each of the three launches. As can be seen, the first flight was somewhat atypical with lower apogee and lower peak reentry velocity which probably resulted from the considerably shorter firing times for the third and fourth stages. In addition, the overall timing from launch was at variance with the other two flights and also with some Ohio State University Trailblazer II launches (Caldecott et al, 1967; Caldecott and Bohley, 1968). In general, however, the overall flight performance for the three vehicles is quite similar.



(a)



(b)

Figure 2. Typical Nose Cone Configurations Showing Dimensions and the Location of the Experimental Instrumentation: (a) cutaway view, second flight and (b) external view, third flight

Table 1. Vehicle and Flight Parameters for the Three Flights

Property	Flight I	Flight II	Flight III
Launch	1532 hrs (EDT) 18 Jun 1967	2156 hrs (EDT) 17 Jun 1969	1900 hrs (EST) 24 Nov 1970
Payload Weight	64.65 lb	74 lb	70.65 lb
$W/C_D A$	79 lbs/ft <sup>2</sup>	90.4 lbs/ft <sup>2</sup>	86.3 lbs/ft <sup>2</sup>
Spin Rate	8 rps	12 rps	11 rps
$I_T$	1.094 slug ft <sup>2</sup>	1.049 slug ft <sup>2</sup>	0.924 slug ft <sup>2</sup>
$I_A$	0.471 slug ft <sup>2</sup>	0.470 slug ft <sup>2</sup>	0.510 slug ft <sup>2</sup>
Center of Gravity (Distance from Nose)	10.0 in.	9.17 in.	9.76 in.
Apogee	902,183 ft	964,395 ft	990,548 ft
Peak Velocity	16,593 fps (at 220kft)	17,287 fps (at 220 kft)	17,972 fps (at 216.5 kft)
Initial Angle of Attack	12°48'	15°28'	10°6'
Reentry Flight Azimuth	357.5°(estimate)	286°	31°
Time From Launch to Reentry (300 kft)	392.7 sec	404 sec	405.4 sec
Third Stage Burn Time	29 sec	38.5 sec	40.8 sec
Fourth Stage Burn Time	5 sec	6 sec	9.4 sec
Initial Coning; Allowed Value	3.45 rps	5.37 rps	5.53 rps
S-Band Trans- mitter	Stagnation	Stagnation and Shoulder	Shoulder
S-Band Receiver	Shoulder	Shoulder	Shoulder
Electrostatic Probes	2-Nosecap; 1-side	2-Nosecap; 1-Side	Stagnation; Nosecap; Side
Electroacoustic Probes	Nosecap; side	2-Nosecap	---
Conductivity Probes	---	---	Shoulder
Strip Line Probe	---	---	Shoulder
Telemetry at Base of Cone	X-Band	S-Band	S-Band



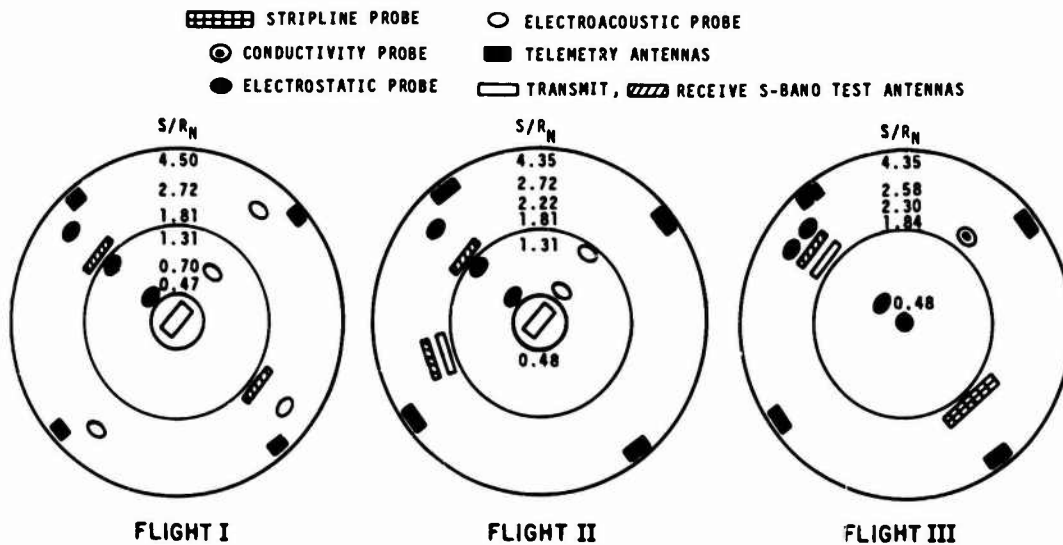


Figure 3. Head-on View of the Three Flight Nose Cones Showing the Locations of the Various Elements on Each Vehicle Surface

## 1. FLIGHT RECORD FROM GROUND RADAR

### 1.1 Radar Trajectory

The flights are monitored by a number of ground radar sites. The quality of the tracking data from each station is evaluated, and the best results are used over any given portion of the trajectory. For the first flight, the Spandar S-band and AN/FPS-16 C-band results were used during some periods but most of the data was from the AN/FPQ-6 C-band radar. The AN/FPQ-6 radar was used for almost the entire second flight. Most of the third flight trajectory was determined from Spandar data. At the fourth-stage ignition point, however, it became highly unreliable. The only force acting on the vehicle at that time was gravity, so the trajectory should have been smooth. The radar estimated velocity components, however, showed spurious accelerations in the form of large scale oscillations. Based on this tracking failure, the AN/FPQ-6 data for that portion of the flight were re-examined. It was found that this radar was able to provide much better results during the fourth-stage burn. Unfortunately these records were only available up to 397 sec, around 440 kft. Since there was no reliable information beyond that point, it became necessary to determine the velocity and trajectory by extrapolation. Inasmuch as the final rocket firing had been completed and atmospheric drag could be neglected, the nonvertical velocity components were frozen and acceleration in the altitude component was assumed to be due to gravity only. Once vehicle drag becomes a significant factor, however, this approach must be modified. On the previous flights which had comparable operating

conditions, the vehicle velocity peaked around 220 kft. This indicates that the drag was then sufficient to counter the acceleration of gravity. As the vehicle continued to descend, it underwent further deceleration from the increased atmospheric density. It was assumed that the present flight followed this trend and hence the simple approach could not be extended below 220 kft.

Since the oscillations in the velocity components were no longer apparent, the use of the radar data was once again considered. With this in mind, the assumed portions of the velocity profiles were faired into the new radar values. The results are shown as the dotted line of Figure 4. The curve for the Flight II case, which was for quite similar conditions, is crossed by the Flight III curve using the radar data. This unlikely result led to closer examination of the velocity curves for the three flights. For this purpose, the curves were replotted in Figure 5 as a function of altitude rather than time. The anomalous crossover is

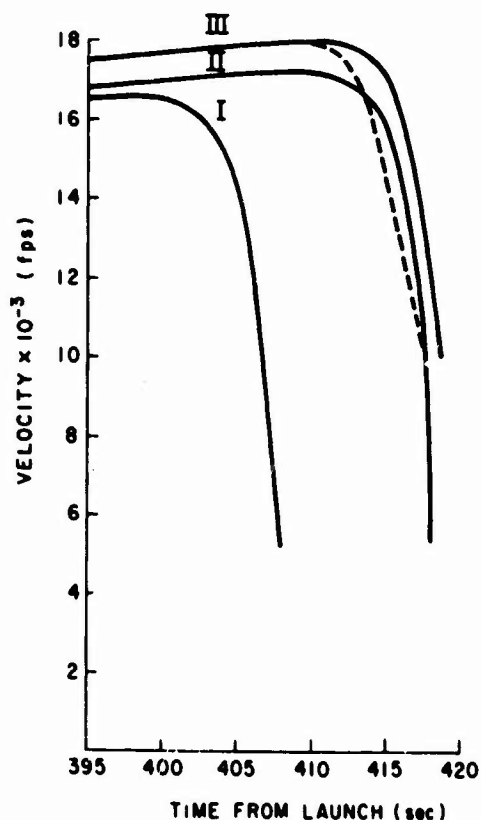


Figure 4. Time History of the Reentry Velocity for the Three Flights. There are two sets of third flight values after 410 sec: --- is from radar data, and — is a theoretical estimate

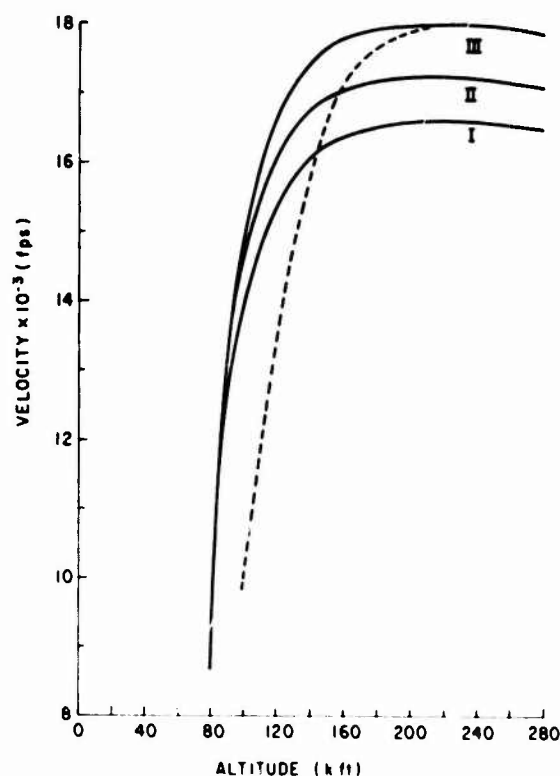


Figure 5. Variation in Vehicle Velocity During Reentry With Altitude for the Three Flights. The --- portion of the third flight curve again represents the radar data

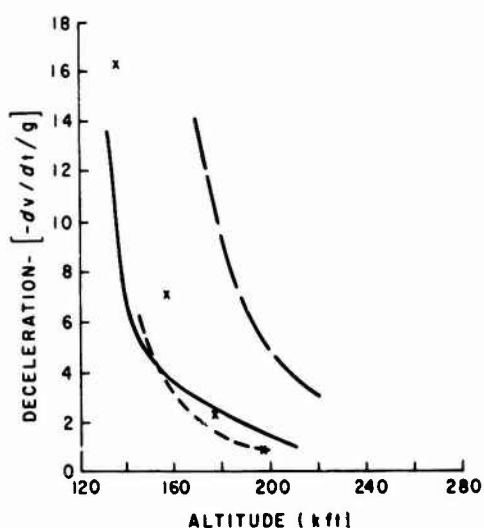


Figure 6. Vehicle Deceleration:  
flight II - ——— ; flight III - — — —  
radar data, - - - - accelerometer data,  
and (x) semiempirical results

large decelerations at the high altitude range. These are unlikely and are clearly incompatible with the accelerometer data. It is these deceleration values which produce the crossover seen in Figure 5. The above considerations have a twofold significance. First, they offer further confirmation of the need to reject the radar data. Secondly, the agreement between the second flight and the accelerometer establishes a condition which the velocity determination must satisfy.

The simplified velocity formulation was now extended to include drag. The altitude velocity component was assumed to change according to the relation:

$$\frac{dV_{ALT}}{dt} = g - \frac{\rho V_{ALT}^2 C_D A}{2m}.$$

If an exponential decay of density is assumed, this gives:

$$\frac{dV_{ALT}}{dt} = g - \left( \frac{\rho_0 C_D A}{2m} \right) V_{ALT}^2 e^{-\beta y}.$$

Use of simple drag coefficient and base area of the vehicle, however, led to values of deceleration which were too small. One factor in these results is that the vehicle was at an angle of attack. Thus the simple reference area did not really

still present and has become more exaggerated. At this point the renewed use of the radar was discarded as a feasible solution and another approach had to be sought. The selection of a semiempirical method to include drag effects needs some discussion.

Since deceleration activated switches were to be employed on subsequent flights, an accelerometer was included on the third flight to establish expected levels over the altitude range from 200 to 140 kft. This information has been included as a curve in Figure 6 which displays the vehicle deceleration for the second and third flights based on the radar data. The second flight curve shows excellent agreement with the accelerometer readings of the third flight, while the corresponding radar curve for the third flight shows

apply. An empirical correction factor was then employed. This had its basis in the assumed agreement between this flight and the previous ones as far as the altitude at which its peak velocity should have occurred. A suitable pseudo-area was introduced to provide sufficient drag to produce the proper deceleration near 220 kft. The deceleration history based on this new velocity profile can also be seen in Figure 6. This is in far better agreement than the Flight III radar data. The velocity results are shown as the solid line extensions of the third flight curves in Figure 4 and Figure 5. The degree of similarity in the profiles for the three flights that appears in Figure 5 is especially encouraging as justification for this approach. It should perhaps be noted that if the Flight III radar data for position are considered rather than velocity then there is better agreement between

the radar values and those resulting from an integration of the calculated velocity history. This is shown in Figure 7. Indeed, at the very low altitude range the curves for the first and second flights show trends which more closely resemble the radar data of the third flight than the calculated values. That the calculated values should disagree here is not surprising, since they are based on a fitted curve biased toward agreement at higher altitudes. In addition, the radar may have overcome tracking fluctuations and returned to the actual trajectory. The velocity-time-altitude histories of the three flights are summarized in Table 2.

Table 3 presents a comparison of the various radar parameters at three altitudes. Recall that although the positional data may be representative for the third flight, the velocity values are not. The events of the first flight all occur at much earlier times and the peak velocity is lower. Nevertheless, the overall profiles are similar as can be seen in Figure 5. The second flight represents essentially the predicted vehicle performance, while the third flight velocity

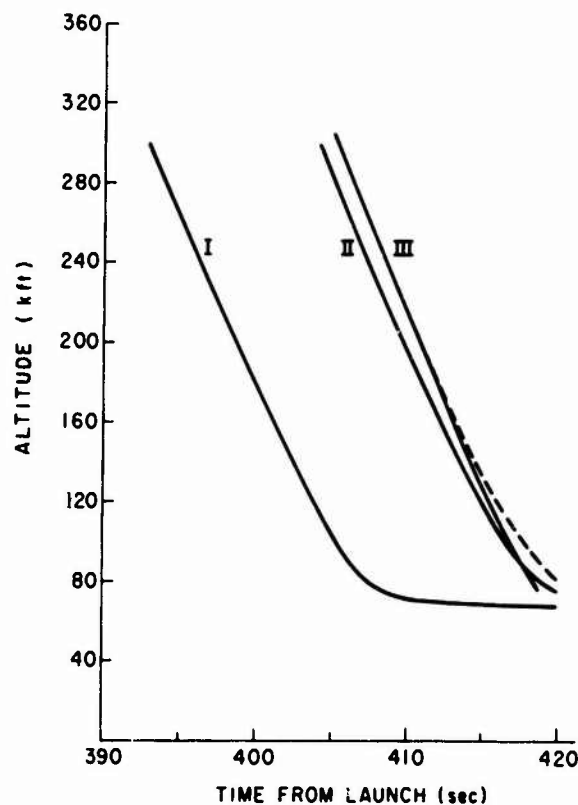


Figure 7. Vehicle Altitude as a Function of the Time-from-Launch for the Three Flights. The third flight uncertainty is again shown below 170 kft: --- radar, and — estimated

Table 2. The Altitude-Time-Velocity History for the Three Flights (Based on Radar Data)

Altitude (kft)	Date				By	
	Flight I		Flight II		Flight III	
	Velocity (fps)	Time (sec)	Velocity (fps)	Time (sec)	Velocity (fps)	Time (sec)
500	†uncertain	380.1	16,768	392.0	17,464	393.9
480	15,548	381.4	16,810	393.2	17,486	395.0
460	16,122	382.7	16,834	394.4	17,517	396.2
440	16,204	383.9	16,867	395.6	17,557	397.3
420	16,260	385.2	16,920	396.8	*17,603	398.4
400	16,285	386.5	16,974	398.0	17,641	399.6
380	16,347	387.8	17,005	399.2	17,675	400.7
360	16,358	389.0	17,014	400.4	17,720	401.8
340	16,377	390.3	17,047	401.6	17,747	403.0
320	16,450	391.5	17,091	402.8	17,783	404.1
300	16,470	392.8	17,106	403.9	17,823	405.3
280	16,497	394.0	17,143	405.1	17,859	406.4
260	16,526	395.3	17,169	406.3	17,899	407.6
240	16,559	396.5	17,208	407.5	17,930	408.7
220	16,593	397.7	17,287	408.7	17,965	409.8
200	16,560	399.0	17,238	409.8	17,965	410.8
180	16,510	400.2	17,130	411.0	17,940	411.9
160	16,381	401.4	16,983	412.2	17,800	413.0
140	16,070	402.7	16,841	413.4	17,500	414.1
120	15,366	404.0	16,100	414.6	16,650	415.4
100	13,775	405.4	14,633	415.9	15,000	416.8
80	8,682	407.2	7,815	417.6	*10,500	418.3

† End of fourth stage burn  
for this flight (atypical).

\* Extrapolated values.

Table 3. Radar Data for the Three Flights at Typical Altitudes

(a) Flight I			
Property	Altitude		
	500 kft	150 kft	100 kft
Slant Range (ft)	976,915	773,656	754,724
Azimuth (deg)	151.2568	148.6901	148.2824
Elevation (deg)	29.6204	10.1167	6.6120
Horizontal Range (ft)	820,003	747,577	737,556
Velocity (fps)		16,251	13,775
Latitude (deg)	35.8586	36.0788	36.1098
Longitude (deg)	-74.1658	-74.1801	-74.1817
North-South Range (ft)	-723,565	-643,455	-632,171
Look Range (ft)	969,960	765,370	746,300
East-West Velocity (fps)		-164	-132
North-South Velocity (fps)		3,685	3,100
Flight Elevation (deg)			
Visual Azimuth (deg)	151.9201	149.3869	148.9837
Look Azimuth (deg)	151.9201	149.3869	148.9837
Look Elevation (deg)	29.9066	10.2505	6.7103
East-West Range (ft)	385,900	380,655	379,992
Altitude Velocity (fps)		-15,827	-13,421
Flight Azimuth (deg)			
(b) Flight II			
Property	Altitude		
	500 kft	150 kft	100 kft
Slant Range (ft)	976,203	813,066	800,175
Azimuth (deg)	167.4551	160.4291	160.1628
Elevation (deg)	29.6616	9.5259	6.1132
Horizontal Range (ft)	820,279	789,479	785,383
Velocity (fps)	16,768	16,888	14,633
Latitude (deg)	35.7576	35.7972	35.8027
Longitude (deg)	-74.4387	-74.6100	-74.6339
North-South Range (ft)	-761,321	-747,358	-745,423
Look Range (ft)	970,146	806,712	793,846
East-West Velocity (fps)	-2,500	-2,472	-2,090
North-South Velocity (fps)	700	632	589
Flight Elevation (deg)	-81.09	-81.27	-81.47
Visual Azimuth (deg)	158.1341	161.1913	161.6364
Look Azimuth (deg)	158.1741	161.2016	161.6429
Look Elevation (deg)	29.8847	9.6193	6.1796
East-West Range (ft)	305,433	254,481	247,379
Altitude Velocity (fps)	-16,565	-16,692	-14,471
Flight Azimuth (deg)	285.65	285.42	285.73

Table 3 (Contd.) Radar Data for the Three Flights at Typical Altitudes

(c) Flight III			
Property	Altitude		
	500 kft	150 kft	100 kft
Slant Range (ft)	984,410	750,304	726,891
Azimuth (deg)	153.3924	153.1505	153.1116
Elevation (deg)	39.3308	10.4526	6.9676
Horizontal Range (ft)	825,148	720,504	706,073
Velocity (fps)	15,684	15,969	13,910
Latitude (deg)	35.7988	36.0606	36.0966
Longitude (deg)	-74.2434	-74.3898	-74.4101
North-South Range (ft)	-737,724	-642,955	-629,888
Look Range (ft)	999,735	767,517	744,255
East-West Velocity (fps)	-1,925	-1,894	-1,682
North-South Velocity (fps)	4,172	4,205	3,689
Flight Elevation (deg)	-72.96	-73.22	-73.06
Visual Azimuth (deg)	153.3747	153.1634	153.1295
Look Azimuth (deg)	154.7059	154.6519	154.6434
Look Elevation (deg)	28.7884	10.1653	6.7539
East-West Range (ft)	369,716	325,219	319,079
Altitude Velocity (fps)	-14,996	-15,289	-13,306
Flight Azimuth (deg)	335.23	335.75	335.49

exceeded original estimates. The radar returns indicate erratic performance near 70 kft and some vehicle deterioration is assumed to have occurred around this altitude.

### 3.2 Vehicle-Ground Orientation

All three vehicles are launched in a generally southeastern direction. Once apogee has occurred, the third and fourth stages separate from the ballistic path and enter almost vertically. Depending on vehicle orientation during firing, however, different north-south and east-west velocity components are imparted. This can be seen from the flight azimuthal entries in Table 3. Based on these values, the projection of the vehicle trajectory on the earth plane for the first flight is aligned almost due north; for the second, it is between west and northwest; while for the third, it is in a northeasterly direction.

This suggests the question of dispersion for the Trailblazer II payloads during their reentry. The position of the three vehicles with respect to the launch point at successive altitudes is shown in Figure 8. Despite the large vertical component in their velocities, the vehicles are not at all close. An additional feature of this figure is that the orientation of the vehicle flight paths with respect to the main base and the subsidiary stations, ADAS and Coquina Beach, can be seen. This is related to the reception of vehicle transmissions on the ground. But before

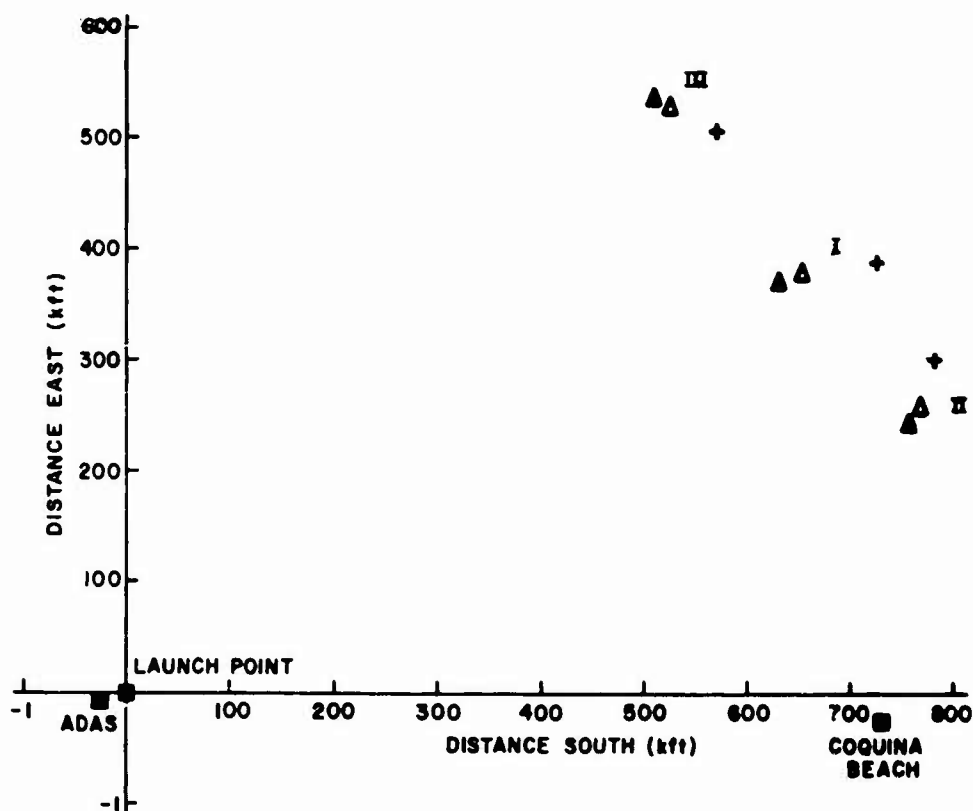


Figure 8. Geographical Orientation of the Three Vehicles to the Ground Stations During Descent at Altitude of (+) 500 kft, ( $\Delta$ ) 150 kft, and ( $\blacktriangle$ ) 100 kft. The vehicle dispersion would be represented by a circle with radius of 35.5 miles

turning to this question, it is first necessary to discuss another aspect of this problem; namely, the spin, precession, and angle of attack associated with the nose cone.

### 3.3 Spin

On the first two flights, the spin rate was determined from the rate of change in the radiation pattern of the S-band transmitting antenna located in the vehicle nose. Since the radiated fields were linearly polarized, the spin caused the signal received at the ground stations to oscillate from a maximum (when the polarization vectors were aligned) to a minimum one-quarter revolution later (when they were orthogonal). The periodicity of the signal shortly after fourth-stage firing indicated that the vehicle spin rate was 8 rps in the case of the first flight, and 12 rps for the second flight. On the third flight, all the antennas were located on the side of the



vehicle and thus a different approach was used. At lower altitudes where plasma effects were present, periodic variations in the electron density levels—seen by the electrostatic probe located at  $S/R_N = 2.58$ —established the cyclic rate associated with the vehicle. At higher altitudes, however, the lack of electrons made it necessary to use information from a shoulder antenna. Since the vehicle was spinning about its axis, the orientation of this antenna with respect to the ground receiving stations was continuously changing. Because the electron density was still at free space levels, it was possible to conclude that any periodic variations in received signal intensity—as monitored by the automatic Gain Control Recorder—were due to the spin. Analysis of these data indicated an 11-rps spin rate for the flight period following fourth-stage burn.

### 3.4 Precession and Angle of Attack

Two types of precession must be considered in establishing the orientation of the Trailblazer II nose cone. The first possible effect is an initial coning motion about an arbitrary axis which could be induced by the separation from the third-stage, or by thrust deviations during the fourth-stage firing. The other is an externally induced coning due to aerodynamic forces tending to realign the vehicle with the velocity axis that appears only after the atmosphere becomes sufficiently dense. The approach of Caldecott et al (1967) was followed in verifying the presence of either or both precessions from the flight data of the three launches.

#### 3.4.1 INITIAL CONING

The magnitude of the factors inducing any possible initial precession would not affect the rate of the coning motion, but only the relative position of the axis of the precession. The rate of this precession is determined by the properties of the vehicle; the precession rate is given by

$$\phi = I_A \omega / I_T$$

where  $I_A$  is the longitudinal moment of inertia,  $I_T$  is the transverse moment, and  $\omega$  is the angular spin velocity. The allowed value for each of the flights is given in Table 1. The presence of initial coning would cause the cyclic variations of the signal intensity to exhibit a modulation at the corresponding rate for that vehicle. The data used to obtain the spin rates were again examined for evidence of this type of fine structure. Neither the antenna patterns nor the AGC data for the three flights showed any such variation at the prescribed frequency.

The absence was also confirmed by the electrostatic probes. The recorded value for the electron density in the plasma over their respective locations alternately indicate maxima and minima. The variation corresponds to the change

in plasma seen by the probe due to the spin and angle of attack of the vehicle. Any other perturbations in the vehicle motion due to precession about an arbitrary axis would appear in the results: successive maximal (or minimal) levels would not be identical; the variations would follow the calculated cyclic rate for the precession. There was no evidence of this effect.

Figure 9 shows the combined effects of spin and precession based on the electrostatic probe results. There are no data on the precession at altitudes below the cutoff point where the probe current saturates. This varies for each flight depending on plasma conditions at the particular probe location. At first, only the constant spin variation is present. Then the action of atmospheric forces gradually decreases the time between maxima (increases the frequency). It should be noted that although the curve for the first flight indicates some slight divergence from the spin value at an earlier altitude than the others, the quantity of the probe data on that flight is exceedingly poor in this region and hence the precise altitude at which the precession begins is somewhat uncertain.

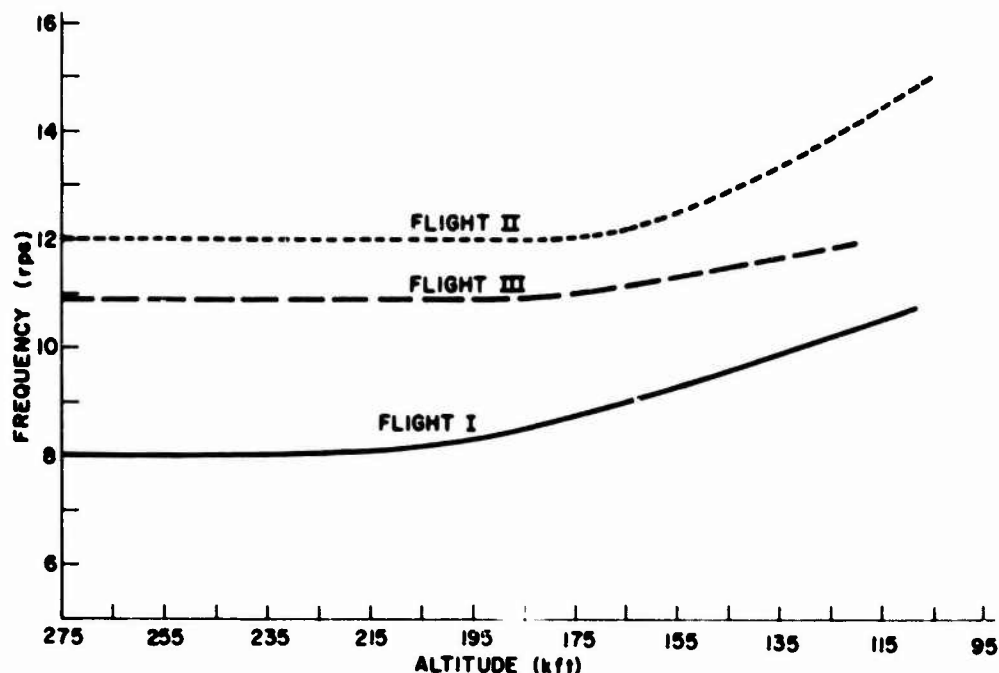


Figure 9. Frequency of Cyclic Variations in the Test Data. This corresponds to the combined effect of spin and precession on the time between maximal values as a function of altitude

The basic conclusion of interest here is that the coning effect due to initial misalignment either was not present or was of such small magnitude that it had no measurable effect on the sensors.

### 3.4.2 INITIAL ANGLE OF ATTACK

Since there was no indication of significant initial coning for any of the three flights, each vehicle's spin axis can be considered to be aligned with the direction of thrust during the respective fourth-stage accelerations. Then, as long as no significant forces disturb this orientation, the angle of attack associated with the reentry can be determined by calculating the angle between the acceleration vector and the velocity vector.

As a result of the poor quality of the radar data during the fourth-stage firing, the velocity components before and after the burn were plotted. The separation between the resulting levels in each case was taken to be proportional to the total acceleration in that component direction due to the fourth-stage thrust. These magnitudes were then normalized to obtain the direction cosines for the acceleration vector. The direction cosines of the velocity vector were next found and the angle of attack determined by calculating the angle between the two vectors based on their direction cosines. The results for the three flights are presented in Table 1.

### 3.4.3 AERODYNAMIC PRECESSION AND DECAY OF ANGLE OF ATTACK

Because of their interdependence, the two topics of aerodynamic precession and decay of vehicle angle of attack will be considered simultaneously. The results for the vehicle spin rate (Figure 9) confirm that there was an extended period when the electrostatic probes detected significant ionization levels in the flow with no variation in the time between successive maxima and minima. This implies that for that range there were no aerodynamic forces acting to compress the angle of attack.

The general question of the interrelationship of these two factors was studied using two different models. The first approach was based on that of Leon (1958). This involved the general case of a spinning vehicle. The solution for the angle of attack envelope is presented in the form of a ratio of the actual value to that obtained by setting the spin parameter  $k_3 = 0$ . For large spin Leon obtains the result:

$$\frac{\text{Env}\{\alpha(y)\}_{k_3 \rightarrow \infty}}{\text{Env}\{\alpha(y)\}_{k_3 = 0}} = \frac{\left( \frac{\alpha E}{\sqrt{\pi} k_2^{1/4} e^{-\beta y/4} \left( \frac{1}{k_3^2} + \frac{1}{4k_2 e^{-\beta y}} \right)^{1/4}} \right)}{\left( \frac{\alpha E e^{\beta y/4}}{\sqrt{\pi} k_2^{1/4}} \right)} \sqrt{\frac{\pi}{2}} \left( \frac{1}{k_3^2} + \frac{1}{4k_2 e^{-\beta y}} \right)^{-1/4}.$$

Because his solution employs expansions of Bessel functions with large argument, the restriction is placed on the result that the term involving the static stability parameter  $k_2$  must be large. This restricts his approach to altitudes where large deceleration effects are present and angle of attack convergence is to be expected.

In order to describe conditions at higher altitudes, the alternative solution was examined. This followed the work of Allen (1957) and is restricted to a non-spinning vehicle. Analysis of the results of the two formulations was used to develop the overall angle of attack history.

Figure 10 shows the oscillatory decay of angle of attack based on Allen's development. This employs the cosine approximation to the Bessel function. The exact solution at a number of altitudes is also indicated. As expected, the agreement is excellent at low altitudes but above the altitude corresponding to the first finite bound on the Bessel function of zero order, the approximation is no longer completely valid and the solutions begin to diverge. For our cases, this represents an altitude of between 185 and 190 kft. Although Leon's solution also depends on the large argument of the Bessel function, he uses his results to indicate the envelope of the solution only and—as can be seen in Figure 10—this still applies although the specific values differ. Thus as an overall indication of the bounds on the angle of attack for a nonspinning vehicle, the results obtained should still be reasonable even at the higher altitudes.

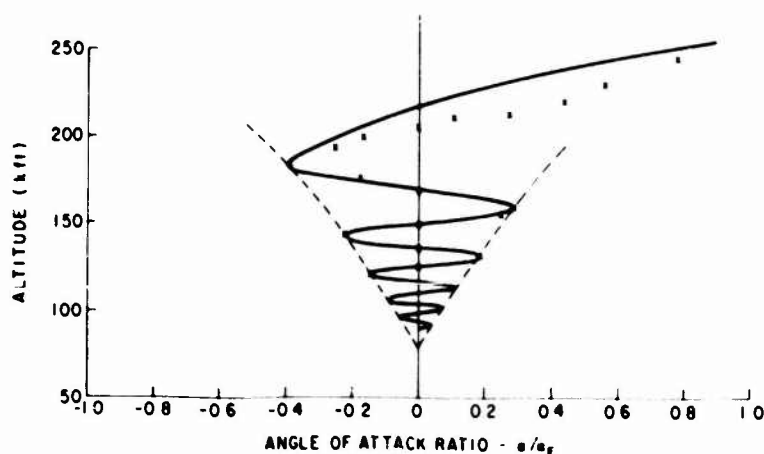


Figure 10. Altitude Decay of Normalized Angle of Attack,  $\alpha/\alpha_0$ , Using Allen's Theoretical No-Spin Formulation: — solution by cosine approximation, and (x) actual Bessel function values

Figure 10 describes the Allen results in terms of

$$\frac{\alpha}{\alpha_E} = e^{k_1 y} J_0 \left[ 2k_2^{1/2} e^{-\beta y/2} \right]$$

and for large argument this becomes

$$\alpha/\alpha_E \approx \left[ e^{k_1 y} \cos \left( \frac{\pi}{4} - 2 \sqrt{k_2} e^{-\beta y/2} \right) \right] / \sqrt{\pi \sqrt{k_2} e^{-\beta y/2}} .$$

We can compare his envelope solution

$$\left( \frac{\alpha}{\alpha_E} \right)_{\text{NO SPIN}} \approx \left( \frac{1}{\sqrt{\pi} k_2^{1/4}} \right) \left( e^{k_1 y} \cdot e^{\beta y/4} \right)$$

to Leon's. Indeed if we consider limiting cases for the dynamic and static stability parameters,  $k_1$  and  $k_2$ , such that  $k_1 e^{-\beta y} \rightarrow 0$  and  $\beta C_{L\alpha} \sin \theta_E \rightarrow 0$  in the expression for  $k_2$ , then Allen's result has the equivalent form to Leon's nonspin case:

$$\text{Env } \{\alpha(y)\}_{k_3=0} \sim \frac{\alpha_E e^{\beta y/4}}{\sqrt{\pi \sqrt{k_2}}} .$$

Since these limits are reasonable for the present vehicle and flight conditions, the agreement between the two formulations supports the validity of Leon's results even at higher altitudes than is strictly justified.

The decay of the angle of attack envelope for spin and no-spin conditions, using the flight parameters for each launch, can be seen in Figure 11. It is clear that despite variations in the three sets of values for spin and stability parameters, the decay is virtually the same in all cases.

If in addition to the decay of the oscillation envelope, the complete history is examined to determine the time or altitude change associated with one period of the motion, then the effect of aerodynamic forces on this oscillation can be seen. These results appear in Figure 12 which compares observed and predicted behavior for the three flights. The semiempirical curves represent the use of actual flight velocities rather than the theoretical velocity decay. The matching is poorest for the first flight, tending to confirm the lack of reliability in the observed flight data for the electrostatic probe. The low altitude results for the theoretical case

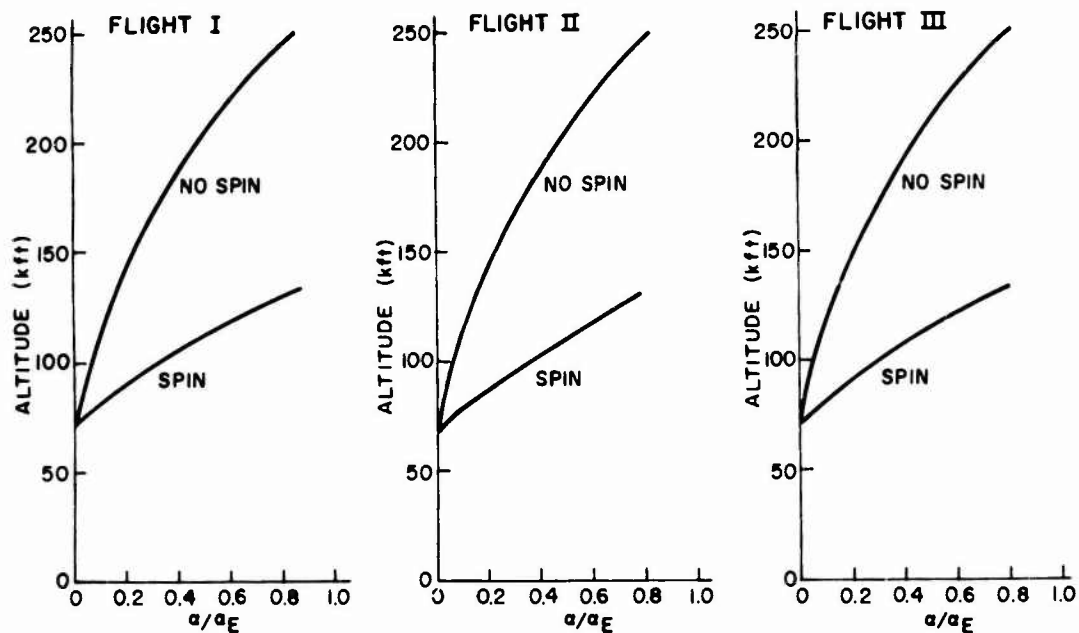


Figure 11. Decay of Angle of Attack Based on the Inclusion of Flight Data in Leon's Formulation Assuming That the Vehicle Has and Does Not Have Spin

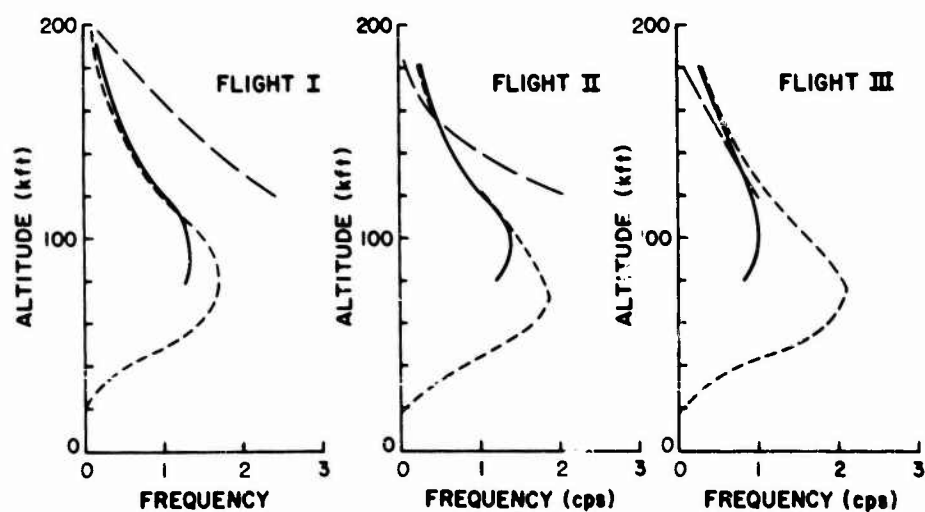


Figure 12. Precession Frequency as a Function of Altitude for the Three Flights: --- theoretical, — — observed, and — — semi-empirical

diverge from the empirical and flight results. The theory predicts that the frequency of oscillation will peak at approximately 75 kft, whereas using radar determined flight velocities in the calculation results in peak values near 100 kft. This indicates that the simple angle of attack decay, using an exponential density profile, does not represent a completely adequate formulation over the entire range of the reentry.

### 3.5 Transmission Angles

Once the vehicle orientation has been established, this information is used in analyzing the S-band antenna patterns received by the ground stations. The ADAS and Main Base radars are quite close to each other, while Coquina Beach is located some distance to their south and west. This means that the analysis of the signals received by the ground stations must take into account transmission angle differences for each location. Several angles are defined for the three flights and their values are shown in Table 4. The angles designated as  $\alpha_{ij}$  are between the vehicle velocity and axis vectors or between either of these vectors and the various ground stations, while the  $\theta$  values are for the angle between the ground station radius vector to the vehicle and the local vertical on the earth's surface. Figure 13 shows the relative position of these vectors for each flight. Note that since the vehicle enters almost vertically, the velocity vector is not distinguished from the earth vertical. From Table 4 it can be seen that although there is considerable variation in angles from one flight to the next, the particular

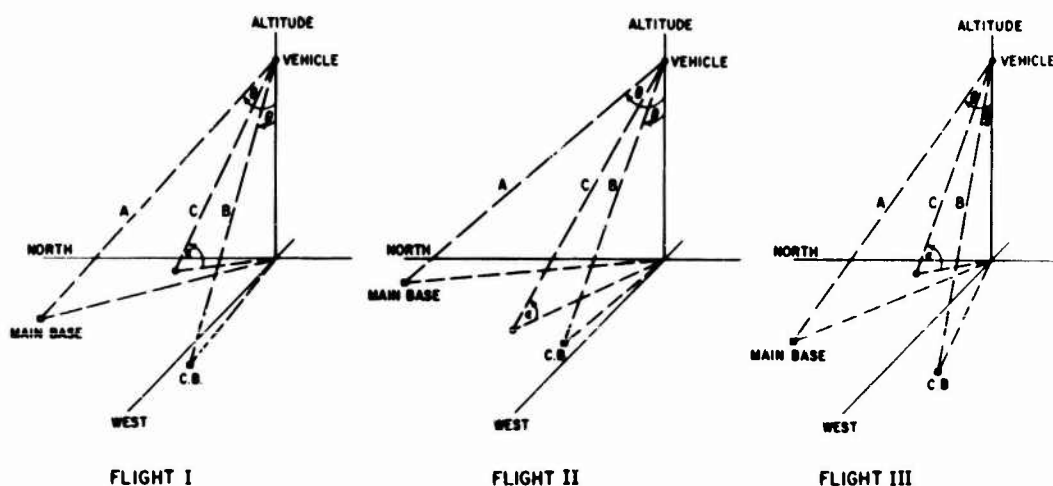


Figure 13. Typical Orientation of the Transmission Vectors for the Three Flights During Reentry: (A) vehicle-main base vector, (B) vehicle-Coquina Beach vector, and (C) vehicle axis vector

Table 4. Transmission Angle Values for the Thru Flights

Angles (°)	Altitude (kft)			
	300	250	200	150
Flight I				
$\alpha_{13}$	57.29	60.81	63.72	67.19
$\alpha_{14}$	57.79	60.81	64.06	67.44
$\alpha_{15}$	56.19	61.19	66.95	72.93
$\alpha_{23}$	43.76	46.81	50.07	53.51
$\alpha_{24}$	44.20	47.18	50.36	53.70
$\alpha_{25}$	56.27	61.00	66.42	72.25
$\theta_3$	68.37	71.98	75.35	78.66
$\theta_4$	69.49	72.52	75.67	79.03
$\theta_5$	54.18	58.91	64.32	70.36
Flight II				
$\alpha_{13}$	64.51	67.74	70.97	74.43
$\alpha_{14}$	65.18	68.33	71.48	74.84
$\alpha_{15}$	36.82	41.60	47.00	53.50
$\alpha_{23}$	49.73	52.90	56.10	59.54
$\alpha_{24}$	50.44	53.53	56.64	59.99
$\alpha_{25}$	30.33	34.53	39.61	45.94
$\theta_3$	69.73	72.57	75.93	79.12
$\theta_4$	70.08	73.16	76.26	79.58
$\theta_5$	45.37	49.98	55.36	62.02
Flight III				
$\alpha_{13}$	63.71	67.25	70.93	73.70
$\alpha_{14}$	64.09	67.55	71.15	73.82
$\alpha_{15}$	67.19	71.64	76.36	80.89
$\alpha_{23}$	54.70	58.21	61.91	65.60
$\alpha_{24}$	54.96	58.40	62.02	65.51
$\alpha_{25}$	67.78	72.18	76.83	81.43
$\theta_3$	67.68	71.12	75.00	78.54
$\theta_4$	68.22	71.72	75.23	79.00
$\theta_5$	62.06	66.56	71.26	75.91



angle representing any one case does not vary greatly as a function of altitude. Thus, in the analysis of the signal returns, it can often be treated as a constant without significant loss of information.

This completes the overall analysis of the flight performance as determined by the Ground Radars. Before the second major part of the report is considered, however, there remain some additional topics which are related to both areas.

#### 4. HEAT TRANSFER AND TURBULENCE

The flight dynamics of the vehicle for the three flights have been considered. The reentry velocity, angle of attack, and vehicle configuration next must be considered in terms of the interaction between the body and the external flow. Two aspects will be discussed.

##### 4.1 Transition To Turbulence

An estimate can be made of the altitude at which the boundary layer around a zero angle of attack configuration would become turbulent. See Fay and Riddell (1958) for details. By approximating the blunt cone by a semi-ellipse having the same axis ratio a solution can be obtained for the local Reynold's Number in terms of free stream properties:

$$Re_{\theta} = \psi R_B^{1/2} (\rho_{\infty}/\rho_0)^{0.5076} \left( \frac{V_{\infty}}{10^3} \right)^{0.477}$$

where  $\psi$  is a factor for body location and  $R_B$  is the base radius. The criterion  $Re_{\theta} \sim 250$  was used to estimate the altitude at which turbulent flow would be expected for a particular location. The back of the payload would then be turbulent at 120 kft and the shoulder above 110 kft. On the other hand, near the tip of the vehicle the critical Reynold's number was never obtained for altitudes at which the vehicle could still be considered to be functioning. Refinements such as the effect of angle of attack were not considered here, and the principal use of this result was in terms of estimating the heating to which the aluminum heat-sink nose-cap would be subjected. This question of survivability at low altitudes will be discussed in the next section in terms of theoretical calculations and the use of thermocouples in the skin and payload. One other factor should be mentioned. The transition to turbulence also results in a change in the character of the boundary layer, which could have an effect on the reflection and attenuation due to the level of ionization in the surrounding flow field. In the present case,

however, this is not of prime importance since the experimental results terminated prior to this condition.

#### 4.2 Heat Transfer

All three vehicles have used the principle of an aluminum heat-sink noscap as thermal protection for the payload, rather than ablative coatings, so that the objective of making plasma diagnostics in a pure air medium could be achieved. The question then is whether the nose cone can absorb the heat from the external environment during the reentry without deteriorating. The vehicle surface is not subjected to a uniform thermal condition and heat transfer decreases away from the stagnation region for laminar flow conditions. Thus to estimate the heating to which the vehicle would be exposed in the course of the trajectory, consideration of the amount of heat transferred to the nose of the vehicle could serve as upper bound on the overall solution. If the stagnation region of the body is treated as being isolated from the remainder and if under those conditions it could absorb the maximal heat input without melting, then the vehicle as a whole should survive. This conclusion is justified by the uniform thickness of the skin and the fact that the flow remains laminar.

Specifically, the nose cone is 0.06-ft thick. This determines the volume and mass of aluminum to be associated with the given surface area exposed to the heating. Calculation of the resulting noscap temperature rise involved a two-step process with coupled heat transfer and wall temperature equations:

$$\dot{q}_{ST} = \frac{865}{\sqrt{R_N}} \left( \frac{V_\infty}{10^4} \right)^{3.15} \sqrt{\rho_\infty / \rho_o} \left( \frac{H_{ST} - h_W}{H_{ST} - h_{300}} \right)$$

$$T_W = T_o + \frac{A}{\rho c_p v} \Sigma \Delta q$$

where

$$\Delta q = \dot{q}_{ST} \Delta t$$

$$T_o = 300^\circ K$$

and

$$h_W = c_p T_W$$

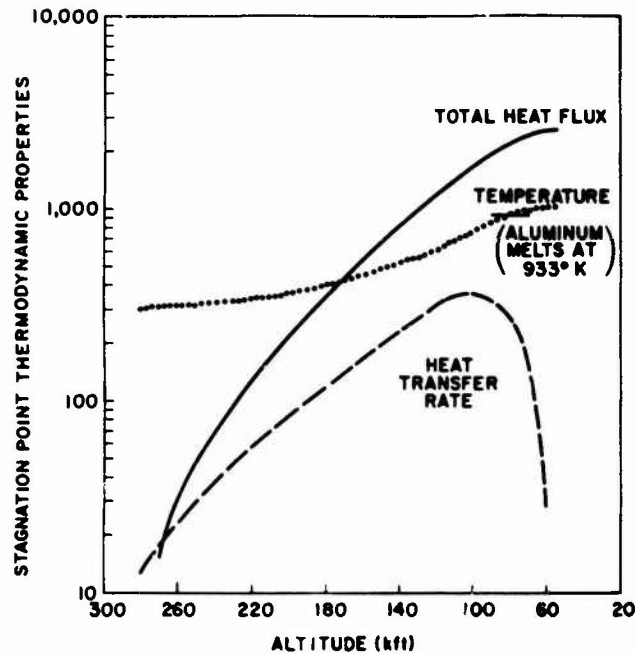


Figure 14. Typical Stagnation Point Heating Properties:  
 — — heat transfer rate, BTU/ft<sup>2</sup>-sec, ——— total  
 heat flux, BTU/ft<sup>2</sup>; and ..... mean wall temperature, °K

It is assumed that the aluminum is a rapid conductor of the external heat and that the skin thickness can be assumed to have uniform temperature. Based on this, the vehicle should still be intact until around 75 kft. Typical results are shown in Figure 14.

## 5. FLOW FIELD STUDIES

### 5.1 General Background

The second major part of this report is concerned with the various predictions of the flow field properties of the ionized reentry environment and in particular, with an evaluation of the adequacy of the theoretical models as confirmed by the results of the flight experiments. The description of this medium during the course of reentry is a highly complex problem due to the variable structure of the flow which is a function of the altitude, velocity, vehicle shape, spin, and

angle of attack. For our purposes, however, a model is considered to be useful if its results agree with some particular observed conditions. As was shown in Figure 3, the three flights were instrumented with a variety of antennas and electromagnetic sensors at different locations on the vehicle surface. The results of these experiments were transmitted to the ground by the telemetry system at the base of the cone. The instruments were designed to measure both integrated and discrete plasma properties. Antenna transmissions to the ground stations provided information about the overall properties of the entire sheath. Reflection and antenna coupling results also require the integration of property distributions. The second type of information was provided by the various probes. Their results are based on properties close to the vehicle surface rather than the plasma as a whole. It should be noted that in some cases, both types of information in conjunction with theoretical analysis could be extended to give additional estimates of plasma properties. Signal attenuation can provide profiles of the flow properties, while data from near the surface can be extrapolated to give properties at the edge of the boundary layer. These derived results are extremely useful in the sense that they allow data from one sensor to provide corroboration for the other. An overall description of the changing experimental environment during reentry will indicate the difficulty in modeling.

The Trailblazer is a blunt hypersonic vehicle which reenters at an angle of attack. The result is a wide variation in flow field properties as the nose cone descends through the atmosphere. At 300 kft, there is no effective plasma. As the ambient density increases, the vehicle velocity causes a diffuse shock to form. Due to the low density, viscous surface effects are apparent throughout the entire region enclosed by the shock. The shock structure gradually compresses and eventually can be represented as a discontinuity. As the altitude continues to decrease, the viscous effects are dominant only in a layer near the vehicle flow interface and the shock layer can be treated as distinct regions with some interaction. Finally, the viscous boundary layer becomes so thin that the interaction is minimal and the flow is almost entirely inviscid. In the course of this whole development, the air passing through the shock becomes heated, undergoing dissociation and ionization. The local species concentrations depend on the history of the chemistry along each streamline in the flow. Given this complexity, the use of different models to obtain solutions for particular cases is a reasonable approach.

The stagnation region behind the normal shock is of considerable importance and was treated in detail. Due to the nose bluntness the shock is detached from the body and a high temperature, high density layer forms behind it. As a result of the chemistry that occurs, this region becomes the major source of electrons for the whole flow. As the ionized gases expand around the vehicle away from

the nose, cooling occurs and recombination becomes the dominant chemical process. In addition, streamlines which enter the shock layer outside the nose region are generally not subjected to the same degree of heating and ionization. The streamline profile in the expansion region thus consists mostly of streamlines which come from the stagnation region coupled with some cool air near the shock. Although recombination has been taking place, convection still represents a greater factor in the electron density around the vehicle than local ionization.

In the expanded region, the viscous boundary layer grows thicker with distance. Thus much of the high temperature air is swallowed into the boundary layer, leaving the inviscid flow as just a cool outer region. Then for many circumstances, especially at higher altitudes, the description of the properties of the boundary layer suffices to determine the effect of the flow on signal transmission. In addition, it should be noted that in general the boundary layer should be laminar rather than turbulent and that three-dimensional effects will be important since the vehicle is at a nonzero angle of attack. The vehicle spin also has an effect since this means that the various sensors will be exposed to the nonuniform features of the flow and will exhibit periodic performance.

The logical starting point in the specific flow analysis is to describe the stagnation region, since nose region effects dominate the entire flow around the vehicle. A considerable amount of experimental data for this region is also available from the flights, so extensive comparisons can be made.

## 5.2 Stagnation Region

Because of the strength of the shock in this region, the high temperature effects become important even at very high altitudes where viscous effects are important. Different solutions were used to account for these features. Their results were then compared with the flight data. On the first two flights these consisted of transmission reflection and coupling antenna results, while for the third flight electrostatic probe data were available.

### 5.2.1 MERGED VISCID-INVISCID SOLUTIONS

In the case of the first flight ( $V_\infty = 16,500$  fps), stagnation region binary scaling from some other results at that same velocity was used as a first approximation. This scaling is valid only so long as binary reactions dominate in the flow, and hence care must be taken near the vehicle surface where three-body recombination cannot be neglected. The curves must be faired in to match equilibrium stagnation point values. The scaling law makes use of the parameter  $\rho_\infty R_N$  which remains fixed under the transformation. For the case of similar velocities, results for a given altitude and body size can be extended to a vehicle

with different dimensions at its corresponding freestream density condition. In applying this approach, equilibrium shock layer thicknesses were assumed. One problem was that there were complications in the fairing-in process due to an electron density overshoot near the stagnation point. Using the curves of Curtis et al (1963), the binary scaling gave results for a number of cases between 200 and 275 kft. Equilibrium stagnation boundary layer results were obtained following the approach of Nerem (1962). In an attempt to describe the conditions represented at these altitudes where distinct boundary and shock layer solutions do not accurately represent the situation, these results were subsequently matched graphically to favor boundary layer values near the body and inviscid results near the shock. As was to be expected, the results were not very realistic at these high altitudes. The built-in requirement of equilibrium properties at the inviscid stagnation point affected the profiles of both the boundary and the inviscid layer. At the higher altitudes where this type of formulation is not valid, this resulted in electron density levels in the plasma sheath which were unrealistically high. The profiles are shown in Figure 15.

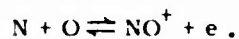
#### 5.2.2 COMPARISON OF MERGED THEORY WITH FLIGHT I DATA

These results were used to analyze antenna performance. When the test results from the first flight were compared to the predictions, the high altitude discrepancies were apparent (see Figure 16). The signal intensity was predicted to decrease at a much earlier point in the flight than actually occurred.

#### 5.2.3 VISCOUS THEORY

The need for better agreement led to the use of more sophisticated flow field calculations at these altitudes. Lew (1970) performed extensive computations for these altitudes at various velocities. He also shows the results of changing the assumptions about conditions in the plasma.

In his formulation, the stagnation flow fields are not divided into a boundary layer and an inviscid regime. Viscous effects are taken to be present over the entire region from the body to the shock front which is considered to have finite thickness. The effects of heat conduction, shearing stress, and diffusion are included at the shock. The chemistry of the high temperature gas behind the shock is considered to be in a state of nonequilibrium. The air species considered are  $N_2$ ,  $O_2$ ,  $N$ ,  $O$ ,  $NO$ ,  $NO^+$  and electrons. The only ionization mechanism is the reaction



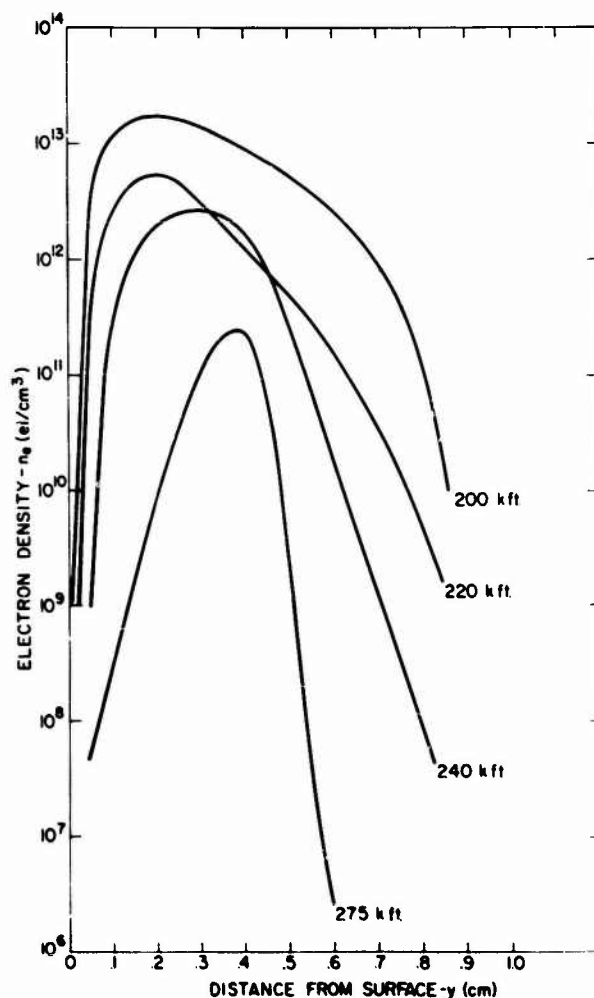


Figure 15. Stagnation Region Electron Density,  
 $V_{\infty} = 16,500$  fps, (Merged Viscid-Inviscid Model)

Moreover, since viscous effects were considered to be important over the entire region, transport phenomena began to play a role in determining the structure of the flow and the shapes of the species profiles. The maximum temperature occurs near the shock interface. As a result of diffusion and convection across the layer, however, electron densities and atomic species concentrations assume their peak values away from the edge of the shock where much of the actual production occurs. Two models were used. In the first model, the vibrational and rotational excitation of molecular species is assumed to have reached equilibrium. In the more advanced version, the restriction of molecular vibrational equilibrium is removed. This introduces significant variations in the

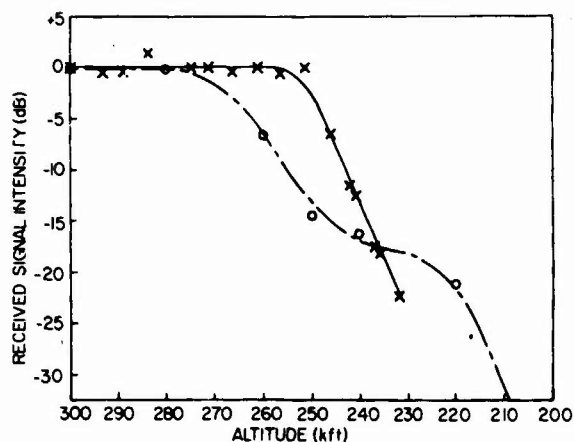


Figure 16. Received Signal Intensity From a Stagnation Region Slot Antenna: (x—x) flight test measurements, and (o—o) model

electron density profiles over the altitude range from 200 to 270 kft. These are shown in Figure 17 and Figure 18. On the other hand, the collision frequency is not greatly affected by the inclusion of vibrational nonequilibrium. The profiles are relatively constant across the shock layer. Figure 19 shows the general trend of the collision frequency. The depicted curves represent vibrational equilibrium results.

The difference between these two models is conceptually simple. The consequences, however, are quite complex. The introduction of a nonequilibrium condition for the vibrational modes has a considerable effect on the electron density of the gas. These changes for the vibrational nonequilibrium case are due to two features: first, the kinetic temperature is higher since the internal heat capacity of the gas is reduced; and in addition, the initial dissociation of  $N_2$  and  $O_2$  is slowed. The higher temperature enhances electron production, but this is in contrast to the lower N and O concentrations available for the associative ionization reaction which tends to lower the electron density. The analysis of the effect on electron production due to the interaction of these two factors, the dissociation rates, and the temperature, serves to explain the complex behavior of the electron density as a function of altitude and velocity.

The first point is that since these differences are due to the inclusion of vibrational nonequilibrium in the model, the effect on the flow properties should diminish as the actual physical system approaches a state equilibrium for these modes. In order to relate this to the present results, the altitude dependence of factors tending to restore equilibrium must be considered. If the collision frequency



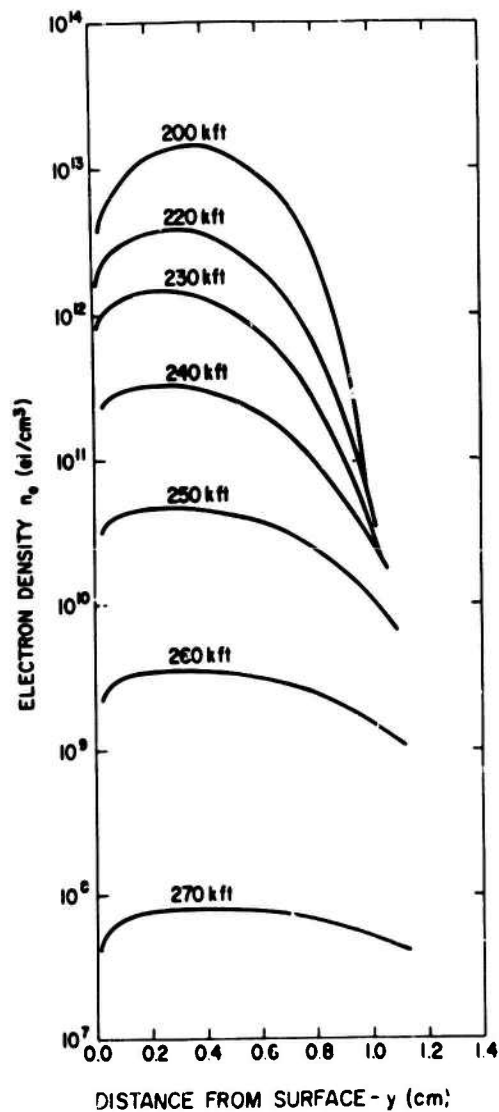


Figure 17. Stagnation Region Electron Density (Vibrational Equilibrium Viscous Model)

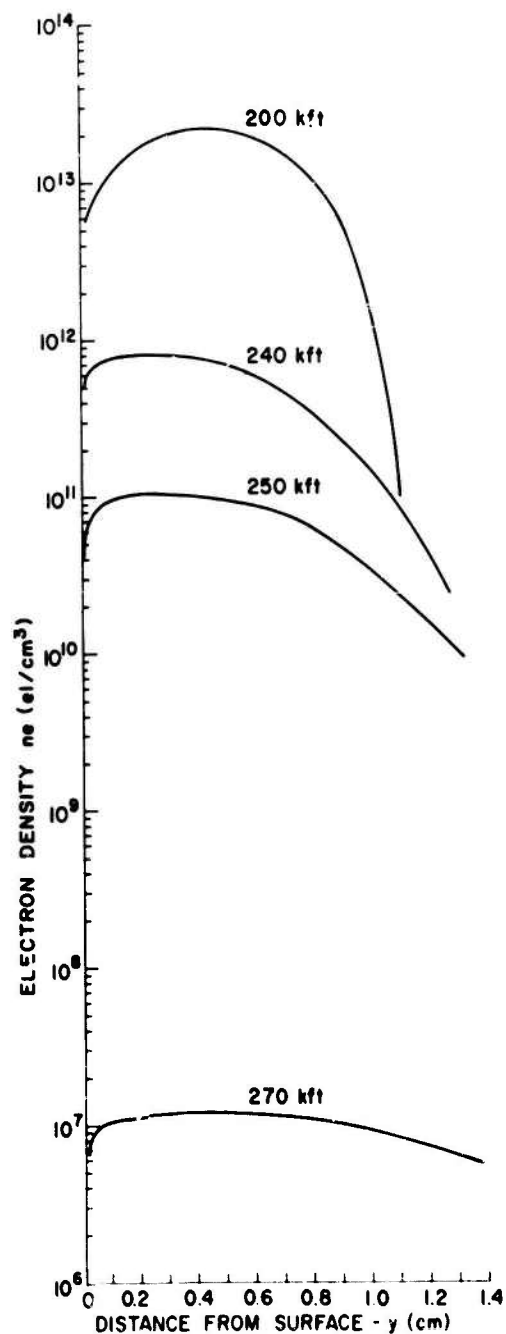


Figure 18. Stagnation Region Electron Density (Vibrational Nonequilibrium Viscous Model)

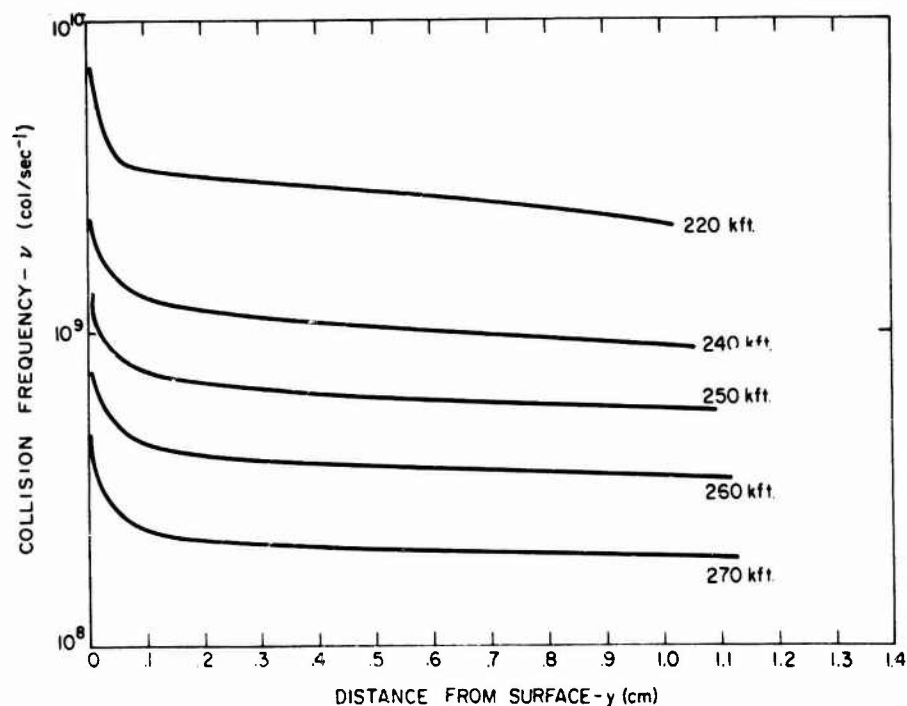


Figure 19. Collision Frequency Profiles in the Stagnation Region,  $V_\infty = 17,500$  fps

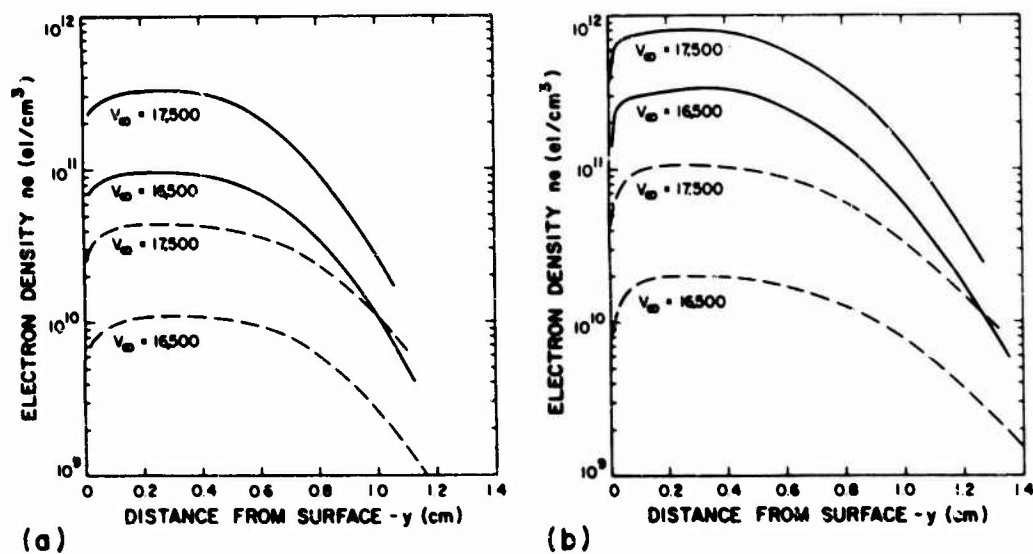


Figure 20. Effect of Freestream Velocity on Electron Density at 240 kft (—) and 250 kft (---): (a) vibrational equilibrium, and (b) vibrational nonequilibrium

is high, the particles undergo more collisions and their energy states tend to reach equilibrium. Increasing the freestream velocity at a given altitude will enhance this by producing a higher density in the gas behind the shock. Figure 20 shows the effect of freestream velocity on electron density profiles at different altitudes for both models. Although the agreement between the profiles at the two velocities clearly varies as a function of altitude, the relationship is complex.

In order to clarify the variational dependence on vibrational nonequilibrium, the altitude history of just the peak electron density as given by the two models is followed for  $V_\infty = 17,500$  fps. This is shown in Figure 21(a). Some results for  $V_\infty = 16,500$  fps and  $V_\infty = 25,000$  fps are included in order to show the effect of the velocity dependence. The differences in the overall profiles for the two models at the same velocity are shown in Figure 21(b) at three selected altitudes. Some of the reasons for this behavior can be seen in Figure 22 and Figure 23 which show the effect of vibrational nonequilibrium on the electron production factors for the  $V_\infty = 17,500$  fps case. Analysis of these factors shows why the two models behave differently as a function of altitude.

First, consider the temperature. Figure 22 shows that over most of the altitude range, the temperature in the nonequilibrium case maintains a rather high value and is essentially independent of altitude. By 200 kft, however, this is no longer true. There, the energy is stored in the internal modes and the kinetic temperature does not differ from that of the vibrational equilibrium model. The other term affecting the electron production mechanism is the dissociation rate. Both atomic nitrogen and oxygen concentrations start at lower levels than they would have under equilibrium conditions, but the nitrogen rapidly surpasses the equilibrium value and rises until there is twice as much present near 240 kft. The oxygen shows a much more gradual rise to the equilibrium concentration. The ratio of vibrational nonequilibrium to equilibrium electron production rates depends on both species concentrations and the temperature. As can be seen in Figure 23, it reaches unity near 260 kft, peaks around 240 kft, and at 200 kft the return to equilibrium levels can be seen. These features can now be applied to the interpretation of the corresponding electron density curves of Figure 21.

The behavior of the electron density for the two models is as expected. The crossover point at which the vibrational nonequilibrium electron density becomes larger than the equilibrium value does occur at higher altitudes when the velocity is increased. This condition then serves as a reference point for analyzing the behavior of the curves for the respective velocity cases. At 250 kft, the  $V_\infty = 16,500$  fps case shows less spread than the  $V_\infty = 17,500$  fps case. On the other hand, near 240 kft, the  $V_\infty = 17,500$  fps solutions are starting to converge while the  $V_\infty = 16,500$  fps vibrational nonequilibrium electron production rate is still increasing with respect to the equilibrium value. Thus, for the vibrational

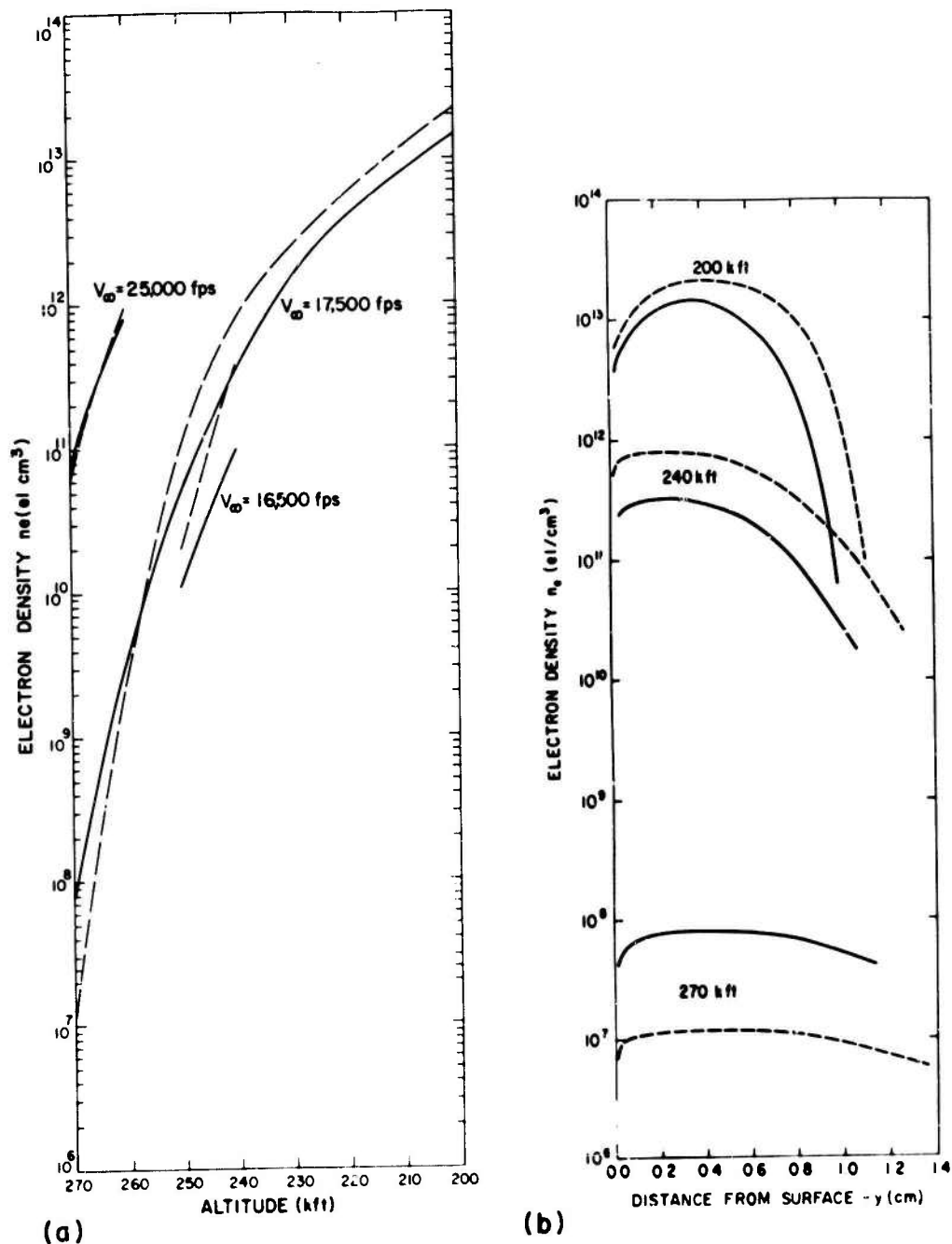


Figure 21. Comparison of Electron Density Predictions as a Function of Altitude: (a) variation of peak values ( $V_\infty$  as a parameter), (b) overall profile at three altitudes. (—) vibrational equilibrium viscous model, and (----) vibrational nonequilibrium model

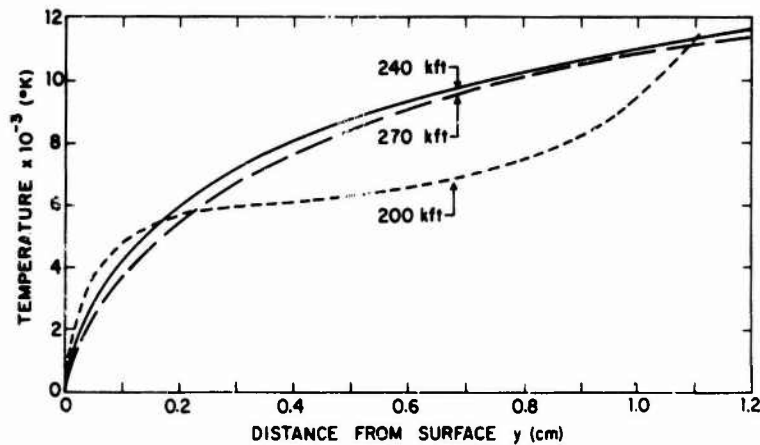


Figure 22. Vibrational Nonequilibrium Temperature Distributions for Three Altitude Conditions

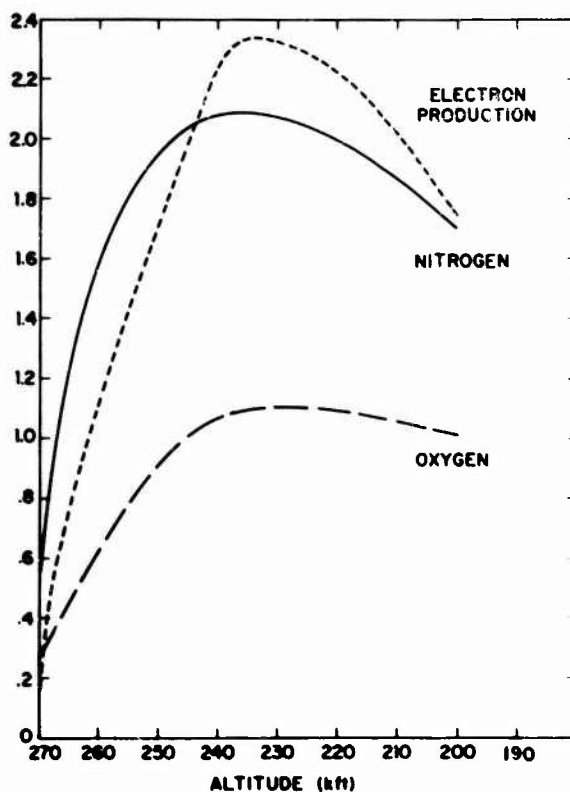


Figure 23. Relative Stagnation Region Peak Atomic Species Concentrations and Electron Production Rates for the Two Models,  $V_\infty = 17,500$  fps: (----) electron production ratio,  $\left[ \frac{(dn_e/dt)_{NEQ}}{(dn_e/dt)_{EQ}} \right]$ ; (—) atomic nitrogen concentration ratio,  $([N]_{NEQ}/[N]_{EQ})$ ; and (— · —) atomic oxygen concentration ratio,  $([O]_{NEQ}/[O]_{EQ})$

nonequilibrium model, results at one velocity cannot easily be extrapolated to represent those of a second velocity condition at the same altitude, except for some highly restricted regions where the results for the two velocities are in phase in relation to their respective crossover points.

Since the overall problem of velocity scaling for the stagnation electron density is so complex, the results covered in Figure 20 through Figure 23 should be given a final summarizing. First, depending on the altitude, a 1000 fps change in freestream velocity can introduce a factor of three or four in peak electron density and this differs at a given altitude depending on the model. Then if the overall profiles are examined, it appears that the vibrational nonequilibrium shock layers extend further from the vehicle surface which affects the flow picture behind the shock. Finally, over the altitude range considered, the complicated nature of the chemical history results in the nonequilibrium peak electron density exhibiting a further order of magnitude variation over the equilibrium.

Although the problem of relating results at two velocities for the same altitude remains unresolved, there are other relationships that can be explored. If consideration is restricted to the vibrational equilibrium model, the altitude variation in peak electron density, Figure 21, represents one such area. The value at 240 kft on the  $V_\infty = 16,500$  fps curve is the same as the 246 kft value for  $V_\infty = 17,500$  fps. Thus, given the identical shape of the vehicle and the relative closeness in velocity, it is worth considering whether the effect of the velocity change can be correlated to a change in altitude. The question to be answered is whether this peak value correspondence is the only agreement for the two cases, or do the profiles of electron density and collision frequency maintain the equivalence for their entire extent.

In Figure 24 the electron density and collision frequency for  $V_\infty = 16,500$  fps at 240 kft are plotted along with a similar set of profiles for  $V_\infty = 17,500$  and 246 kft. These latter results were obtained by interpolation of the various  $V_\infty = 17,500$  fps cases that were available. As can be seen, the results are in excellent agreement over the entire extent of the stagnation region with the slight exception of the tailoff in  $n_e$  near the shock which would not effect experimental predictions seriously. Similar results were found at 250 kft for  $V_\infty = 16,500$  fps, and its matching altitude 256 kft for  $V_\infty = 17,500$  fps. In some cases, then, the effect of velocity can be expressed as an altitude variation.

The various types of theoretical solutions for the stagnation region have been discussed and some relationships among them have been examined. In addition, a comparison has been made between the data from the first flight and the predictions at  $V_\infty = 16,500$  fps using the merged viscous-inviscid model. The poor agreement for this model at high altitudes has been pointed out.

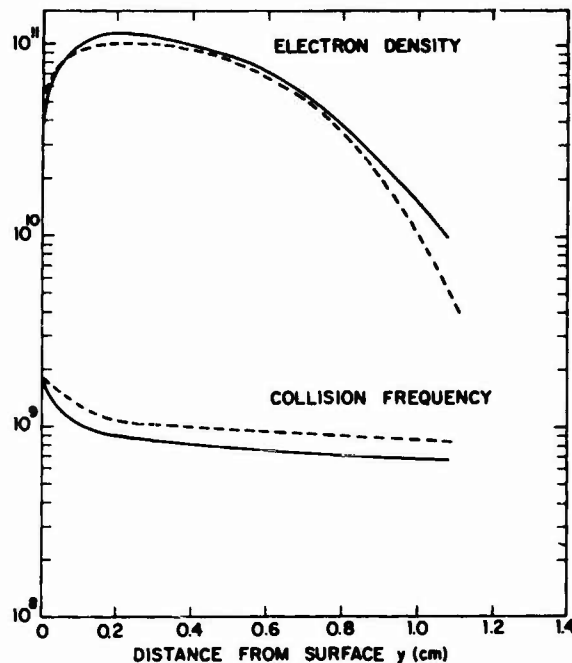


Figure 24. Freestream Velocity as an Altitude Scaling Parameter for Electron Density, ( $\text{el}/\text{cm}^3$ ), and Collision Frequency, (cps): (—) results for 246 kft,  $V_\infty = 17,500$  fps; and (---) results for 240 kft,  $V_\infty = 16,500$  fps.

#### 5.2.4 A COMPARISON OF THE VISCID-INVISCID AND FULLY VISCOUS MODELS

With the more sophisticated theories, it is now possible to make comparisons over a wide altitude range using data from the second flight. This flight had a velocity of 17,500 fps. This is the basic velocity of the viscous solutions but given the difficulties associated with velocity dependence in these sophisticated models, there is a question as to the validity of the comparisons with the results of the more simplified viscid-inviscid calculations made for  $V_\infty = 16,500$  fps. For that type of calculation, however, the prime effect of velocity does not appear in the profile shape but rather in the value for the peak electron density. For the equilibrium conditions at the stagnation point, this is not significantly affected by a 1000 fps change in velocity. For example, at 250 kft for  $V_\infty = 16,500$  fps,  $(n_e)_{ST} = 1.7 \times 10^{12} \text{ el}/\text{cm}^3$  and for  $V_\infty = 17,500$  fps,  $(n_e)_{ST} = 2.0 \times 10^{12} \text{ el}/\text{cm}^3$ . Since this stagnation value dominates the profile, the difference in electron density corresponding to a 1000 fps change in velocity is insignificant for the degree of approximation inherent in this approach. The fallacies in this type of solution at high altitude still apply and hence the main

comparisons should be with the completely viscous results. Some idea of the degree of inaccuracy involved can be seen if the predictions based on the two types of theory are compared.

The most drastic variation is in the peak electron density. In the curves of Figure 15 the peak electron density shows a two order of magnitude change only, compared to the five orders of Figure 17. This is due to the use of an equilibrium stagnation point at the body for the inviscid results. The scaled nonequilibrium values at each altitude had to be matched to the equilibrium stagnation value as has been discussed in the theory. This restriction produces the anomalous results. For instance, at 275 kft the maximum value of electron density was  $n_e = 10^8 \text{ el/cm}^3$  for the region where the binary scaling was valid. This is of the same order as the completely viscous results. For an equilibrium stagnation point, however,  $(n_e)_{ST} = 4 \times 10^{11} \text{ el/cm}^3$  and it is this term which determined the boundary layer values as well as the faired-in portion of the inviscid profile. The curves of Figure 15 indicate the effect this had on the complete profiles for the various altitudes. In the low density cases, the electron density has a sharp rise from the cold wall to its peak value at the edge of the boundary layer. Then there is an abrupt descent to the level predicted by the binary nonequilibrium reactions. This profile result also illustrates the second basic difference in two sets of predictions. The peak electron density for the viscid-inviscid cases occurs near the body in the low velocity stagnation region and it is due to a local production term, whereas in the viscous solutions as discussed above, the electrons are diffused and convected from the production region near the shock and have an internal peak value. This results in a rather uniform profile shape except for the dropoff near the body representing the approach to the catalytic wall boundary condition. Based on these observations, the two theories should always differ in the degree of profile uniformity and in shock detachment distance. At lower altitudes, however, where the binary reaction electron densities begin to approach the equilibrium stagnation level and the boundary layer thickness decreases, the overall agreement between the two solutions should improve.

This pattern can be seen quite clearly in Figure 25. At 250 kft the viscid-inviscid curve is compared to a viscous curve which was also calculated for  $V_\infty = 16,500 \text{ fps}$ . The complete disagreement caused by the stagnation point problem makes clear why agreement at this altitude was so poor in Figure 16. The comparison at 200 kft is between results at the two velocities. Despite this, the curves are quite close in magnitude and show similar profile shapes in contrast to the situation at 250 kft. Since the test results of the first flight implied lower electron densities at the higher altitudes than predicted by the viscid-inviscid theory, Figure 25 can be used as an indication of the quality of agreement expected for the two types of calculation. They should both compare equally well with flight



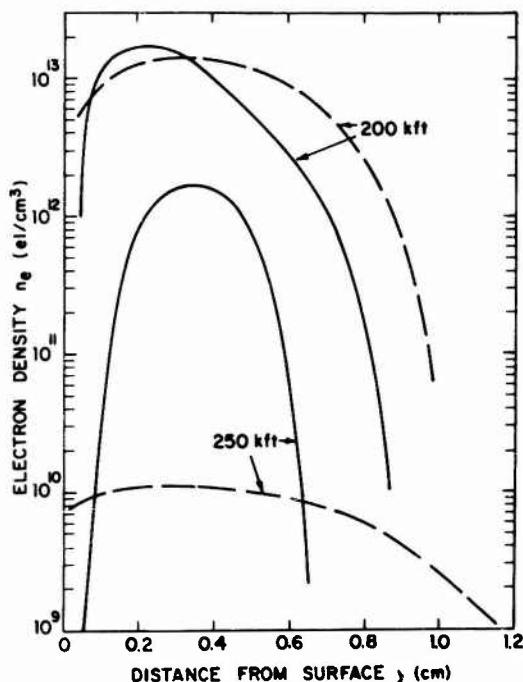


Figure 25. A Comparison of Electron Density Values at Two Altitudes for: (—), the merged viscid-inviscid; and (---), the viscous vibrational equilibrium models

results at 200 kft. Then as the altitude increases, the viscid-inviscid approximation breaks down and its predictions lose validity. On the other hand, the more realistic completely viscous models should still offer reasonable estimates of the flight performance.

#### 5.2.5 FLIGHT II COMPARISONS

Figure 26 shows the received signal intensity from the nose cap antenna during the flight, and the various predictions. It should be noted that this measurement depends on the ground stations; therefore once they lose the signal, no further data are available. For this flight, that point occurred at 240 kft. Therefore, the agreement of the various theories with the actual flight performance below that altitude cannot be determined.

Where there were data, however, the viscous vibrational equilibrium results show reasonable agreement with the signal profile except that a given level of attenuation is assigned to an altitude 8 to 12 kft lower than where it actually occurred on the flight. Introducing the vibrational nonequilibrium formulation brought the results into agreement to within 4,000 ft over the whole range. Within the present knowledge of reaction rate values and the possible atmospheric variations, further refinement for transmission prediction would not be warranted.

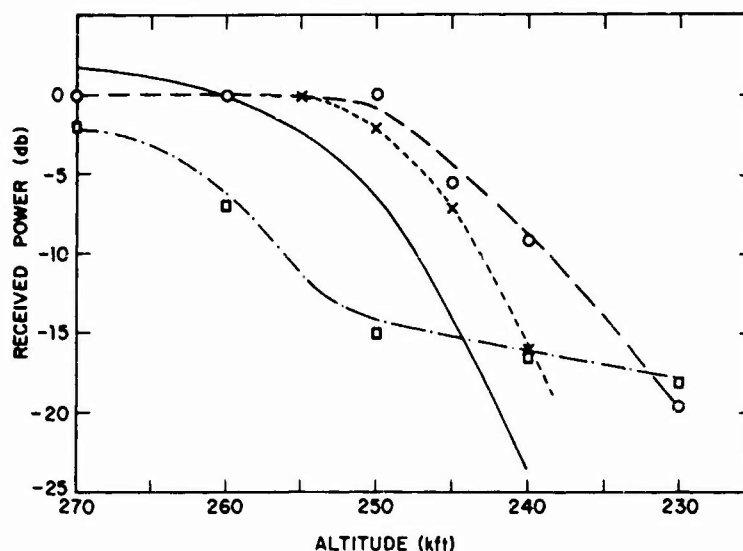


Figure 26. Received Signal Intensity From the Second Flight Nosecap Antenna: (—) flight data; (---) merged viscid-inviscid; (- - -) viscous vibrational equilibrium; and (.....) viscous vibrational nonequilibrium

The complete failure of the viscid-inviscid approximation at high altitudes was again apparent. Despite the higher velocity during the flight, the original predictions still overestimate the attenuation. Furthermore, the results are so inappropriate that they can not even be represented as an altitude shift of any magnitude in contrast to the fully viscous solutions.

The received signal intensity is inversely related to the extent of the region in which the plasma electron density exceeds a critical value. For S-band transmission, this is around  $n_e = 10^{11}$  el/cm<sup>3</sup>. Since attenuation is an integrated effect, both peak value and sheath thickness are involved. The relation between signal intensity and electron density can be seen clearly by considering Figure 25 with Figure 26. For the two viscous solutions, free space conditions prevail about 255 kft. Since this is just below the crossover point, the electron density increases faster for the vibrational nonequilibrium solution below this altitude. This results in the closer agreement of this model with the flight data.

An additional comment about the signal intensity curves (Figure 26) concerns the fortuitous agreement at 240 kft between the viscid-inviscid and vibrational nonequilibrium results. Since the stagnation electron density for the viscid-inviscid case is almost an order of magnitude higher than the binary scaling values, this is well into the altitudes where that scheme is dubious. Indeed, the slope of the attenuation versus altitude curve has already diverged from that of the flight.

The agreement is indicative of the integrated nature of the phenomenon being measured. As can be seen from Figure 15 and Figure 18, two quite different distributions of electrons result in the same degree of signal loss at this one altitude. Both profiles have electron densities above the critical value for most of the flow. The thicker sheath for the vibrational nonequilibrium viscous case is compensated by the greatly higher peak values of the inviscid-viscid calculation. The subsequent disagreement at adjacent altitudes is logical in the light of these two features. At higher altitudes the nonequilibrium profiles fall below critical allowing signal transmission, while the too high peak values of the inviscid-viscid solutions still indicate attenuation. Below 240 kft, the viscous electron density peak increases and the thicker shock results in a higher attenuation which is in agreement with the data. The important result is the excellent agreement with the flight data exhibited by the viscous vibrational nonequilibrium model.

It is possible to use the assumed electron density profiles for further comparisons with flight data in addition to the prediction of attenuation in signal strength as seen by ground stations. Another property associated with a transmitter is the observed power reflection coefficient. This parameter is derived from measurements of incident and reflected power at the input terminals of the antenna. Figure 27 shows the measured reflection coefficient as a function of altitude as well as the correlations with the various flow field model predictions.

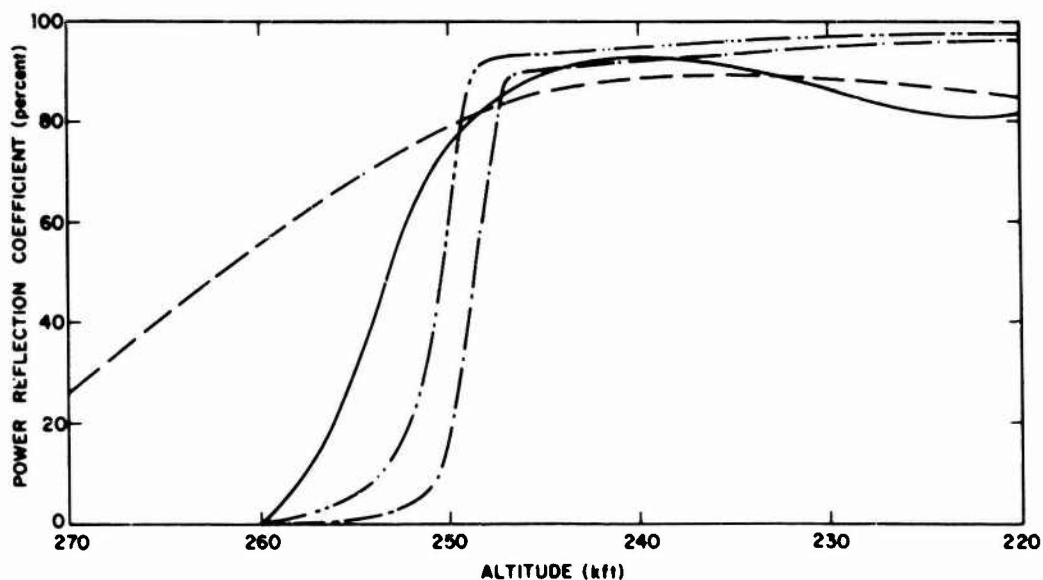


Figure 27. Power Reflection Coefficient for the Second Flight Nosecap Antenna: (—) flight data; (— —) merged viscid inviscid; (— · —) viscous vibrational equilibrium; and (— · · —) viscous vibrational nonequilibrium

Above 260 kft, freespace conditions existed. A sharp rise then occurred reaching almost total reflection by 240 kft. Below that altitude, this condition remained unchanged. The increase in power reflection coefficient is indicative of the plasma becoming overdense. The usefulness of the flow field models depends on their ability to reproduce this history. Once again the viscid-inviscid peak electron densities result in substantial reflections for altitudes well above the flight results. The viscous vibrational equilibrium results show the same rise as the data but at a 10-kft lower altitude. This is the altitude range in which the vibrational nonequilibrium electron densities are higher, and so it is not unexpected that this model predicts increased reflection slightly earlier in excellent agreement with the test results.

At around 250 kft, the viscid-inviscid reflection curve approaches the levels of the vibrational nonequilibrium and flight data curves and then remains in agreement. This represents the regime where most of the power is reflected. Comment has already been made about the disparity in plasma profiles for the viscid-inviscid and viscous models, and Figure 15 and Figure 18 show that for these altitudes the viscid-inviscid profiles have a sloping rise to well above critical  $n_e$ ; beyond that point, there is a considerable extent of overdense plasma. Although overdense, the nonequilibrium vibrational profiles have an extremely sharp rise and reach their high value quite close to the surface. Some explanation for the agreement in results from the two types of profiles was given by a study of the inviscid-viscid profile at 240 kft. The basic electron density distribution was separated into two parts—the overdense portion starting at a point in the plasma and extending outwards, and the rise region between the critical point and the body. A parametric study was then made of the effects due to matching the outer profile to various sets of values in the latter region. Values ranged from insignificant electron density levels to about one half the critical value. Table 5 presents the distributions used and the result obtained. It was found that whatever values were used close to the body, the reflection coefficient in the waveguide agreed within 10 percent. As long as the region of overdense plasma is large, the only factor affecting the reflection is the height at which the layer is raised above the surface. Neither the peak location ( $y \approx 3.0$  cm) nor the properties in the underdense region are significant. The only difference in the two models that would have any effect is that the viscous plasma is critical 0.1 cm out while the inviscid-viscid is 0.5 cm. Based on this, then, it is not surprising that the vibrational nonequilibrium and inviscid-viscid reflection coefficients do not significantly differ in the overdense part of the flight trajectory.

In addition to antenna results in the stagnation region, there are data from a fixed negative bias (-15 V) electrostatic probe which was flown on the third launch. This allowed further comparisons between experimental results and the various

Table 5. Parametric Variation in Electrical Properties of Plasma Layers at Stagnation Point (Altitude = 240 kft)

Model	Slab No. *	Slab Width (cm)	Electron Density $\text{el}/\text{m}^3$	Collision Frequency ( $\text{sec}^{-1}$ )	Dielectric Constant		Power Reflection Coefficient, R
					Real	Imag.	
Standard Profile	1	0.075	0.15E 16	0.10E 11	0.988	0.006	0.725
	2	0.050	0.56E 16	0.10E 11	0.957	0.024	
	3	0.075	0.20E 17	0.10E 11	0.847	0.085	
	4	0.100	0.30E 18	0.10E 11	-1.291	1.288	
	5	0.300	0.22E 19	0.15E 10	-20.950	1.852	
	6	0.075	0.20E 19	0.15E 10	-0.996	0.168	
	7	0.050	0.10E 16	0.50E 09	0.989	0.000	
	8	0.025	0.	0.	0.999	0.	
A	7	0.030	0.50E 17	0.50E 09	0.497	0.014	0.699
	8	0.040	0.30E 17	0.50E 09	0.698	0.008	
	9	0.005	0.	0.	0.999	0.	
B	7	0.030	0.30E 17	0.50E 09	0.698	0.008	0.717
	8	0.040	0.10E 17	0.50E 09	0.899	0.002	
	9	0.005	0.	0.	0.999	0.	
C	7	0.070	0.50E 17	0.50E 09	0.497	0.014	0.679
	8	0.005	0.	0.	0.999	0.	
D	7	0.070	0.10E 16	0.50E 09	0.989	0.000	0.725
	8	0.005	0.	0.	0.999	0.	
E	7	0.070	0.30E 17	0.50E 09	0.698	0.008	0.711
	8	0.005	0.	0.	0.999	0.	
F	7	0.070	0.10E 17	0.50E 09	0.899	0.002	0.722
	8	0.005	0.	0.	0.999	0.	

\* The first 6 slabs for all models are the same as those for the standard profile.

theoretical calculations. The two sets of measurements are independent since the antenna depends on integrated properties across the entire thickness of the plasma sheath, while the probes measure electron density close to the vehicle surface at a distance which varies with the altitude. As has been discussed in previous sections integrated results are more likely to be in agreement, so a match for discrete electron density values at specific locations is an important confirmation of any theoretical prediction. The analysis of the electrostatic probe data and the complex interaction between the plasma and flush mounted probes are discussed in detail by Hayes (1972). The volume of flow from which ions are collected, the pressure and temperature near the wall, and possible convection away from the probe can all effect the current seen by the probe. Results are given for electron density levels at the edge of the sheath within which the ions are collected by

the probe. This thickness is in general quite small and varies with the flow properties at each altitude. Using probes with a negative bias of less than 15 V, Scharfman and Bredfeldt (1967) have shown that positive ion currents could be measured within a factor of two.

Figure 28 shows the probe values for electron density at the sheath edge as a function of altitude. As can be seen, the sheath extends only a short distance above the surface and this decreases rapidly with altitude. In the range from 200 to 260 kft, the electron density as given by the viscous vibrational equilibrium model followed the general trend of the probe but, except for the lower altitudes, the agreement was not within the factor of two. This is not unexpected since the assumption of vibrational equilibrium should become less valid at higher altitudes. When the nonequilibrium is taken into account, the agreement becomes quite remarkable as can be seen in Figure 28. Because of their much more gradual slope near the surface, the electron density profiles of the inviscid-viscid model resulted in predictions at the sheath edge which were far below the flight results and, with the decrease in sheath thickness at lower altitudes, the agreement there became even worse. The end result was a reverse slope for the altitude history.

For 270 kft, the agreement between the probe results and the theoretical values is extremely poor. The vibrational equilibrium model gives an estimate which is two orders less than measured. Since the nonequilibrium results at that altitude are lower than the equilibrium (see Figure 21), there is no improvement in agreement from that model even though its results should be more realistic at that altitude.

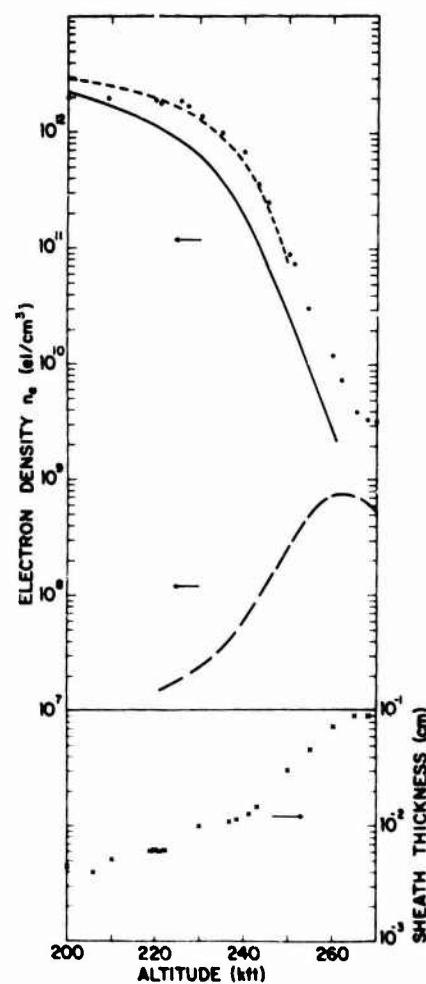


Figure 28. Electron Density and Sheath Thickness for the Stagnation Region Electrostatic Probe on the Third Flight: (•) flight data; theoretical  $n_e$ , (—) merged viscid inviscid, (---) vibrational equilibrium, (-·-·-) vibrational nonequilibrium; and (x) sheath thickness

Attempts were made to improve the probe model to correct for the possibility of convection effects and collection of current from an area larger than the probe face. However these changes represented too small an effect to overcome the discrepancy. Surface catalyticity and other flow theory modifications are being considered; however, since the probe electron density is not only greater than the theoretical sheath values but is also orders of magnitude above even the peak levels of these flow models, this does not look promising. Drastic alterations in either the probe theory or the flow model thus appear to be necessary for the extremely high altitude regime. One further possibility is a parametric study of reaction rates to see if this might improve results.

#### 5.2.6 THE RELATION BETWEEN ELECTROSTATIC PROBE AND ANTENNA DATA

The corroborative experimental correlation is obtained by observing that the microwave power reflection results could be brought into agreement with the vibrational nonequilibrium theory predictions by scaling the latter upward in altitude by some 2,000 ft. Applying this same scaling factor to the predicted nonequilibrium sheath edge electron densities, also brings these values into agreement with the flight values. Thus, there is some degree of consistency between both types of measurements.

#### 5.2.7 SUMMARY OF STAGNATION RESULTS

The vibrational nonequilibrium viscous model gives excellent agreement in the stagnation region for both integrated conditions and discrete electron density descriptions. It is only at the lower altitudes that other models offer equivalent results. While transparent to transmission for the Trailblazer II, the regime above 270 kft does represent the one area where the predictions of local electron density become inconsistent. Attempts to clarify this are being carried out, but in any event the disagreement for those altitudes represents a minor aspect compared to the excellent results obtained for the altitude range where significant electromagnetic phenomena are taking place.

### 5.3 Expansion Region

Up to this point, this report has been concerned with the agreement between calculations and flight test results in the stagnation region. The flights also carried various experimental programs distributed around the side of the vehicles, and the remainder of this report will concentrate on theoretical flow field properties in these regions and the comparison of these results with the experimental data. The effect of angle of attack will be included in the discussion and also some comments on the effect a change in freestream velocity has on the flow properties.

Back around the vehicle, the flow is considered to be represented by an inviscid outer region and a viscous boundary layer close to the vehicle surface. Since a great many of the interesting effects on the various flights occurred during the high altitude regime above 200 kft, this region was given special consideration and the flow properties there received particular attention.

### 5.3.1 HIGH ALTITUDE THEORY

The results in this section come from the computer program developed by Lew (1970) for the solution of high altitude viscous flow. The approach is described in detail in the reference and only a brief outline of some pertinent features will be presented here. In the solution of the flow as it expands around the vehicle, the requirement for completely viscous conditions is relaxed. The flow is considered to consist of the standard inviscid outer region and a boundary layer adjacent to the surface. The solution is iterative. The equations of motion for a chemically reacting flow are integrated along inviscid streamlines, starting at the respective shock conditions and continuing until the resulting mass flux at a given point in the flow matches that of the local boundary layer based on stagnation streamline edge conditions. The new inviscid edge conditions resulting from this match are then used in the solution of the viscous laminar boundary layer equations. The entire procedure is repeated until results are consistent. At these altitudes it has been found that the electron density normal to the surface, as calculated by this approach, has decreased to levels far below critical while still in the boundary layer. This is due to the swallowing of the high temperature flow as it expands. Thus the profiles for the high altitude region do not contain contributions from the inviscid region. In addition, it should be mentioned that in the results presented here for the flow away from the nose the chemical model is restricted to the case of vibrational equilibrium.

### 5.3.2 DISCUSSION OF RESULTS

The variations of the flow properties as a function of location around the body is shown in Figure 29 through Figure 32 as a function of altitude. In all cases the variation in the edge velocity shows an almost linear rise as the flow expands around to the shoulder area and a gradual approach to conical values further downstream. The curves for the maximum and edge temperature show the swallowing of the high temperature flow from the nose. The point at which high temperature effects are no longer at the boundary layer edge varies with altitude, occurring earliest at 270 kft while at 220 kft the external plasma is still a dominant feature around to  $S R_N = 1.0$ . Once the shoulder has been reached, the temperature in the flow remains essentially constant over the rest of the vehicle. The pressure variation also exhibits the change in slope near the shoulder. The transitional



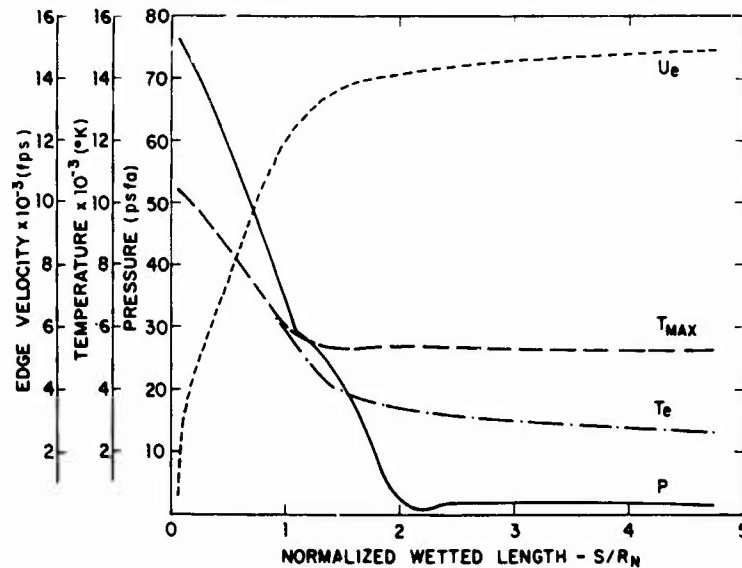


Figure 29. Flow Properties Around the Vehicle for 220 kft and  $V_{\infty} = 17,500$  fps; (—) pressure; (-----) edge velocity; (— · —) maximum temperature; and (— · —) edge temperature

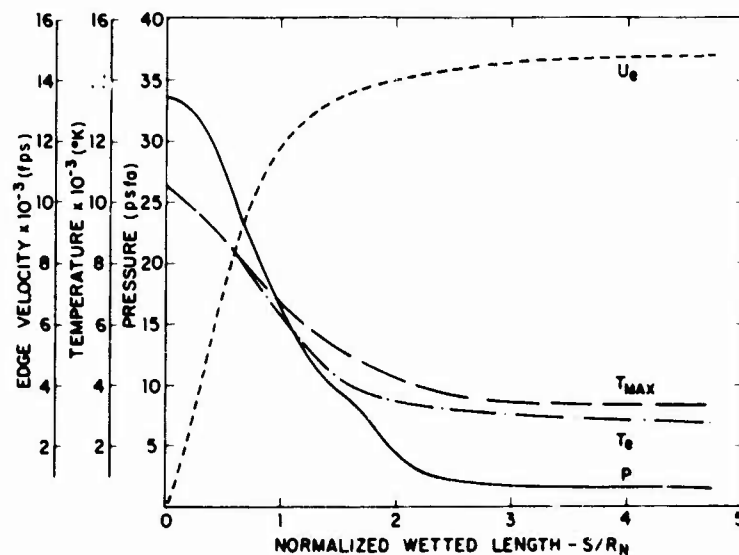


Figure 30. Flow Properties Around the Vehicle for 240 kft and  $V_{\infty} = 17,500$  fps; (—) pressure; (-----) edge velocity; (— · —) maximum temperature; and (— · —) edge temperature

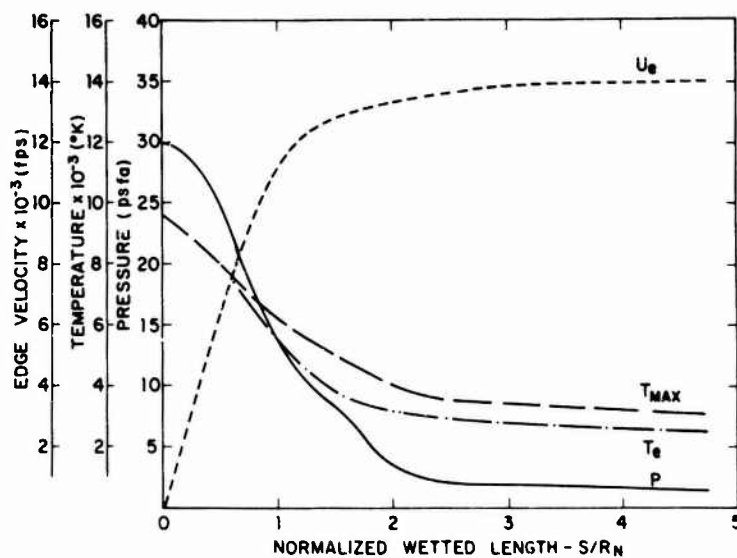


Figure 31. Flow Properties Around the Vehicle for 240 kft and  $V_8 = 16,500$  fps: (—) pressure; (----) edge velocity; (— · —) maximum temperature; and (— — —) edge temperature

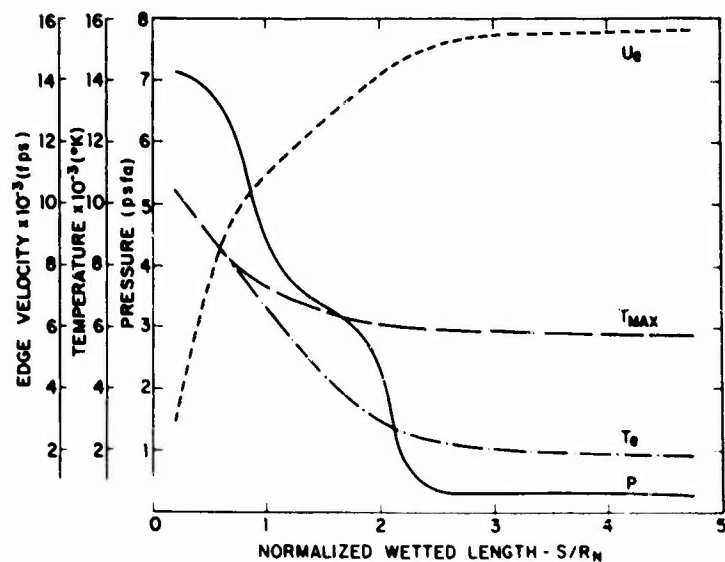


Figure 32. Flow Properties Around the Vehicle for 270 kft and  $V_8 = 17,500$  fps: (—) pressure; (----) edge velocity; (— · —) maximum temperature; and (— — —) edge temperature

effects are especially pronounced at 270 kft, and this will effect the other flow property distributions in this neighborhood. The curves do not approach a constant level until near  $S/R_N = 2.0$ . Further, for the 220 kft case the approach is not monotonic. There is an overexpansion in the pressure followed by a rapid recovery to the invariant level. Figure 33 shows the variation in peak electron density around the body for various altitudes. The peak is always embedded well inside the boundary layer as was pointed out previously. Near the nose, the 270 kft case exhibits a maximum away from the stagnation region, and this is most probably associated with the problem of matching the completely viscous nose solution to a mixed condition around the body. This problem should be especially true at this altitude; since the external expanding flow is still expected to contain viscous effects rather than conforming to the assumed nonviscous constraint of the theory. At the lower altitudes this characteristic disappears and the variation closely follows that of the pressure (including the 270 kft case beyond the peak). There is the change in the slope near the shoulder, and in the 220 kft case the conditions resulting from the overexpansion in pressure produce a sharp decrease below the eventual afterbody level by more than a half an order of magnitude. In all cases as the flow reaches the rear of the vehicle, the electron density has decreased by two orders of magnitude from its peak value.

Since not just peak values but actual distributions of properties across the flow profile are important to the determination of electromagnetic interactions, it is interesting to examine the variation of such a profile as a function of altitude. Figure 34 shows the electron density profiles at  $S/R_N = 1.8$ . Figures 35 through Figure 38 show collision frequency, temperature, density and conductivity of the plasma for the four sets of conditions. The electron density in all cases peaks close to the surface and has dropped an order of magnitude within a normal distance of 6 cm. The temperature always peaks well within the boundary layer and along with the collision frequency and density is relatively constant for most of the flow. An additional feature has been included in these figures, the dc conductivity of the plasma:

$$\sigma = \frac{n_e q^2}{m_e \nu} .$$

Owing to the collision frequency invariance, this follows the electron density profile peaking within a few centimeters of the surface. The conductivity builds up rapidly from quite low values at 270 kft and reaches several mho meter by 220 kft. This will be discussed further, when the experimental results are examined.

Since the peak values around the body and the altitude variation of properties at a single location have been considered, the flow field description can be

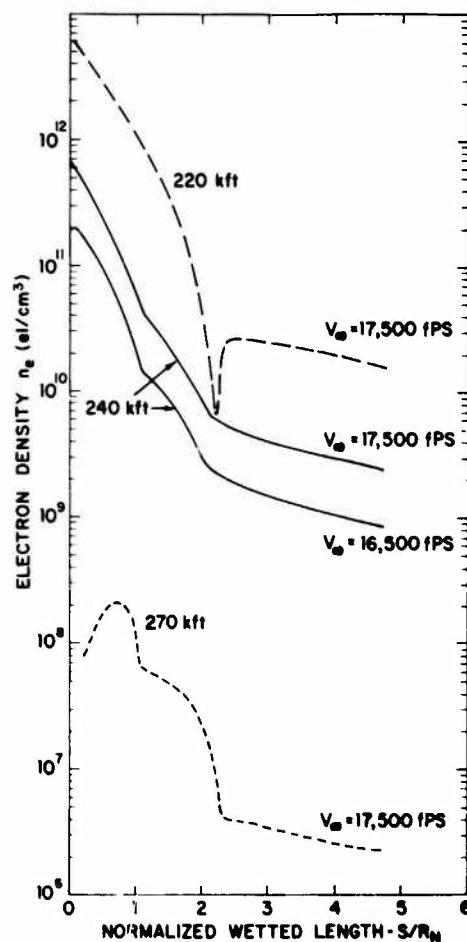


Figure 33. Peak Electron Density Values Around the Vehicle as a Function of Altitude

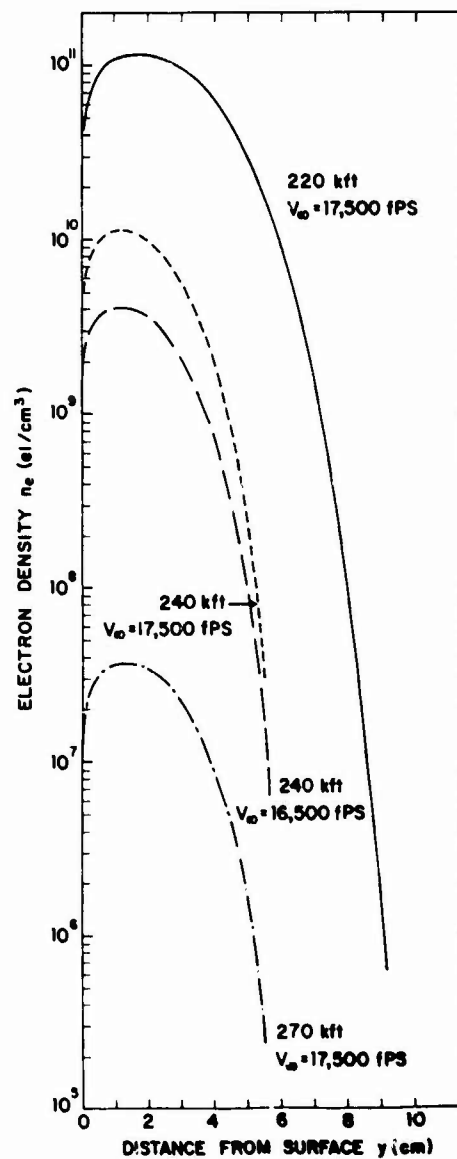


Figure 34. Electron Density Profiles at  $S/R_N = 1.8$  at Various Altitude Conditions

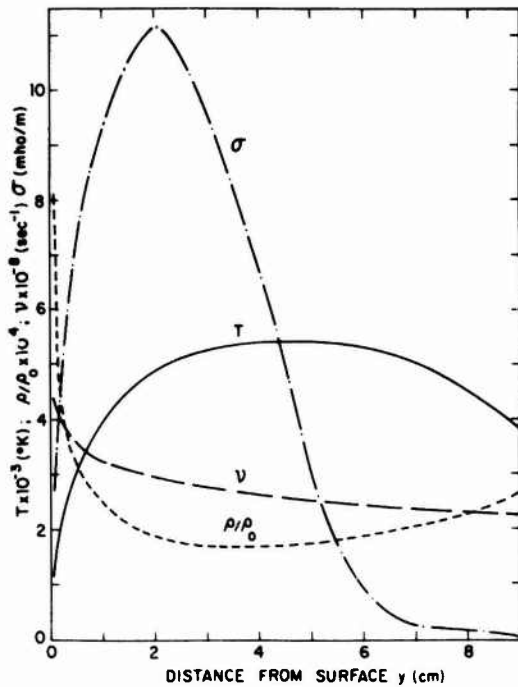


Figure 35. Flow Property Profiles at  $S/R_N = 1.8$  for 220 kft at  $V_\infty = 17,500$  fps: (—) temperature; (-----) density; (— —) collision frequency; and (— · —) conductivity

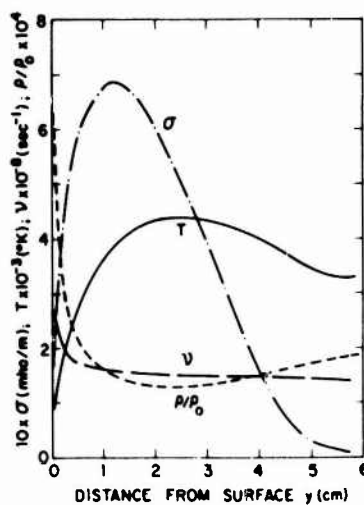


Figure 37. Flow Property Profiles at  $S/R_N = 1.8$  for 240 kft and  $V_\infty = 16,500$  fps: (—) temperature; (-----) density; (— —) collision frequency; and (— · —) conductivity

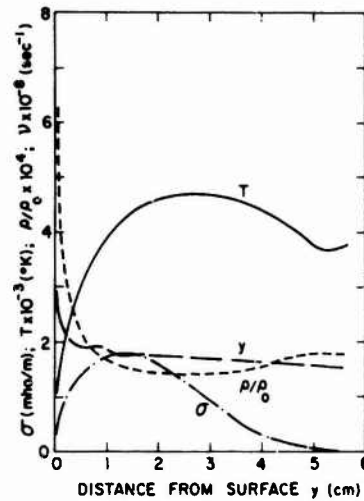


Figure 36. Flow Property Profiles at  $S/R_N = 1.8$  for 240 kft at  $V_\infty = 17,500$  fps: (—) temperature; (-----) density; (— —) collision frequency; and (— · —) conductivity

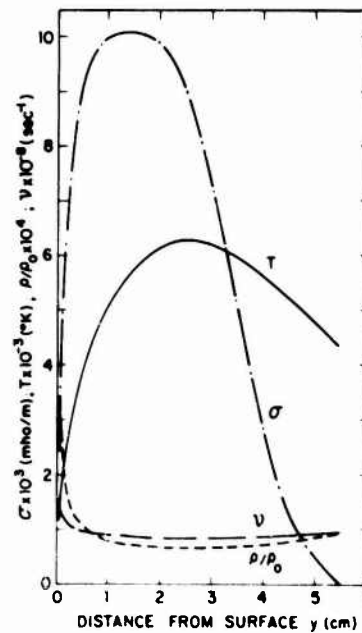


Figure 38. Flow Property Profiles at  $S/R_N = 1.8$  for 270 kft and  $V_\infty = 17,500$  fps: (—) temperature; (-----) density; (— —) collision frequency; and (— · —) conductivity

completed by describing the shape of various profiles at selected body positions for given altitudes. These are shown in Figure 39 through Figure 54. Several features can be observed. There is the gradual decrease in the high temperature, high electron density region as the flow moves back along the afterbody. The relative closeness in the profiles at  $S/R_N = 2.4$  and  $S/R_N = 4.7$  confirms that the flow beyond the former point has approached close to its asymptotic condition. There is a general trend for the profiles to gradually draw closer together as the flow moves along the vehicle. At 270 kft, however, the pattern is drastically altered in the shoulder region. The temperature curves remain unaltered, but the large scale pressure disturbance at the shoulder combines with the temperature to produce a drastic separation in the other flow profiles. Profiles at  $S/R_N = 1.8$  and  $S/R = 1.9$  are compressed until they are practically superimposed on the  $S/R_N = 1.35$  curves. Then on the other side of the underexpansion, the asymptotic trend is normal. Thus there is a major break in the continuity of the profiles for this altitude condition.

One significant feature of all the cases is that even at the rear of the vehicle the flow is still well above 3000 °K in temperature across most of the profile, and hence the electron density can still remain relatively high over the secondary test/telemetry system.

### 5.3.3 ANGLE OF ATTACK

These results are all based on the assumption that the flow is axisymmetric. In actual flight, however, the vehicle was at an angle of attack and hence the flow equations are three dimensional. This type of calculation will not be discussed here, except to note that in general the flow would remain symmetrical while on the hemispherical nose and should exhibit axisymmetric properties only on the conical afterbody. In attempting correlations between theoretical and experimental results, windward and leeward properties at a fixed body location were obtained by using results at positions corresponding to the original  $S/R_N$  value plus or minus the angle of attack of the vehicle. As long as these positions are nose-cap locations with an axisymmetric cross section, the result should be reasonable. Once the flow becomes three dimensional, however, this type of approach which ignores cross flow and shock shape changes should result in poor agreement between theory and experiment.

### 5.3.4 SCALING

There is the question as to the effect of the different reentry velocities for the various flights. Given the moderately blunt hemisphere cone with a velocity in the range of 17,500 fps, a slight change in the external freestream velocity at a given altitude should not be expected to produce a drastically altered shock shape. Further, the elapsed time of flight to a given location in the shocked flow should

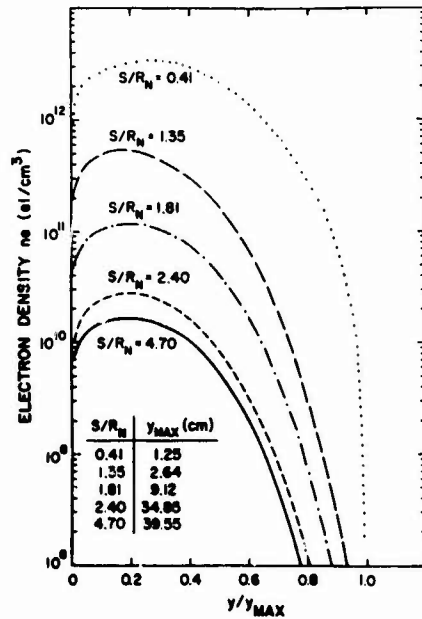


Figure 39. Electron Density Profiles at Various Vehicle Locations for 220 kft and  $V_\infty = 17,500$  fps

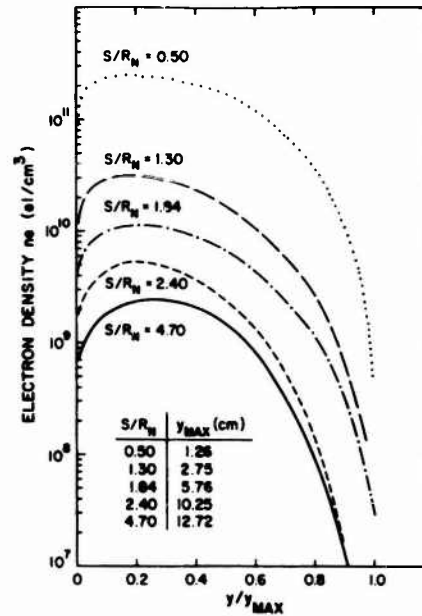


Figure 40. Electron Density Profiles at Various Vehicle Locations for 240 kft and  $V_\infty = 17,500$  fps

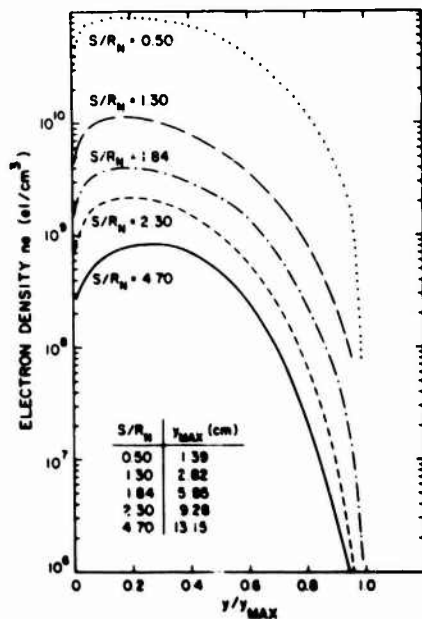


Figure 41. Electron Density Profiles at Various Vehicle Locations for 240 kft and  $V_\infty = 16,500$  fps

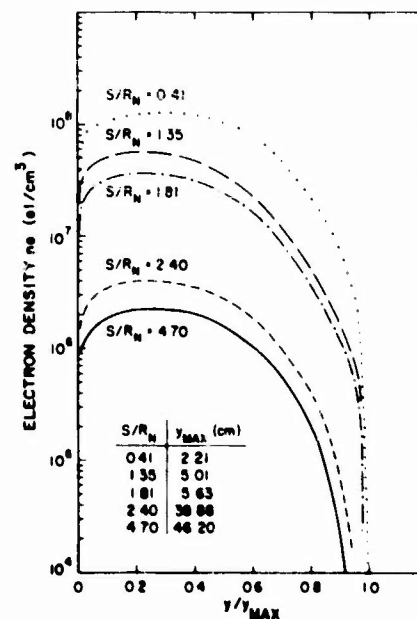


Figure 42. Electron Density Profiles at Various Vehicle Locations for 270 kft and  $V_\infty = 17,500$  fps

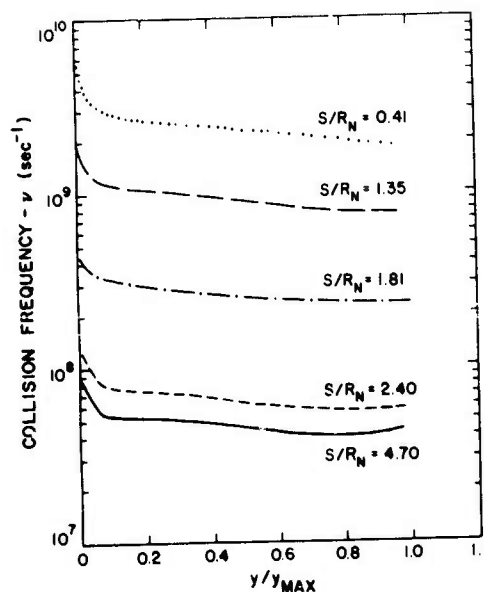


Figure 43. Collision Frequency Profiles at Various Vehicle Locations for 220 kft and  $V_\infty = 17,500$  fps

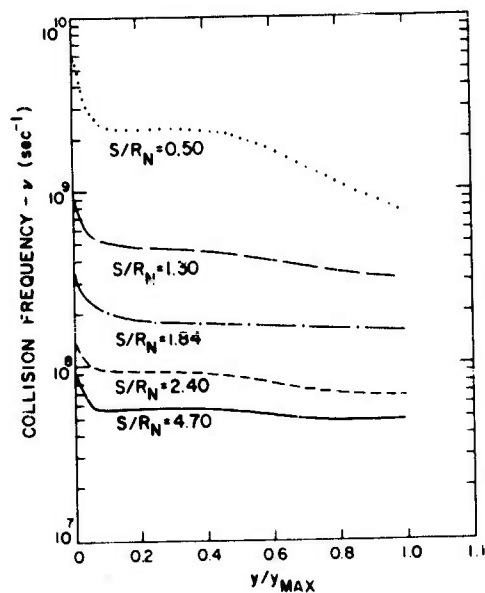


Figure 44. Collision Frequency Profiles at Various Vehicle Locations for 240 kft and  $V_\infty = 17,500$  fps

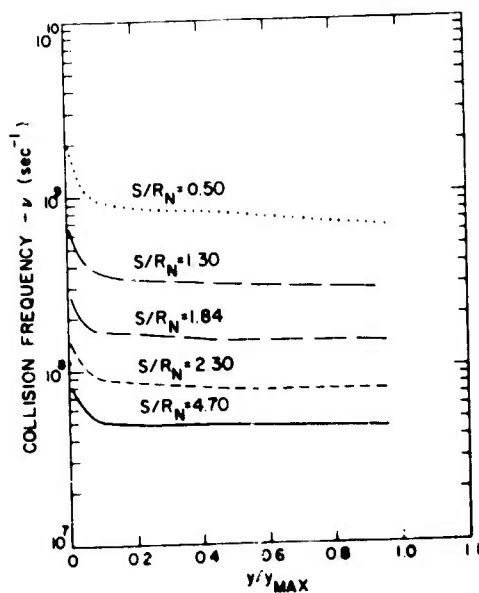


Figure 45. Collision Frequency Profiles at Various Vehicle Locations for 240 kft and  $V_\infty = 16,500$  fps

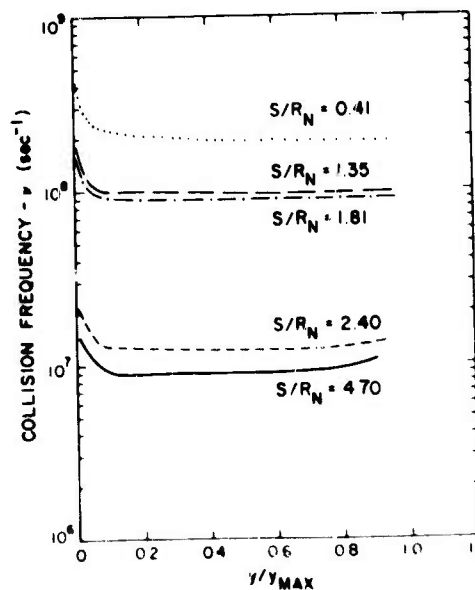


Figure 46. Collision Frequency Profiles at Various Vehicle Locations for 270 kft and  $V_\infty = 17,500$  fps



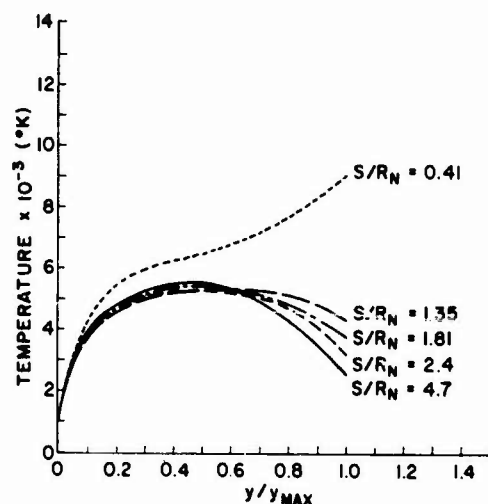


Figure 47. Temperature Profiles at Various Vehicle Locations for 220 kft and  $V_{\infty} = 17,500$  fps

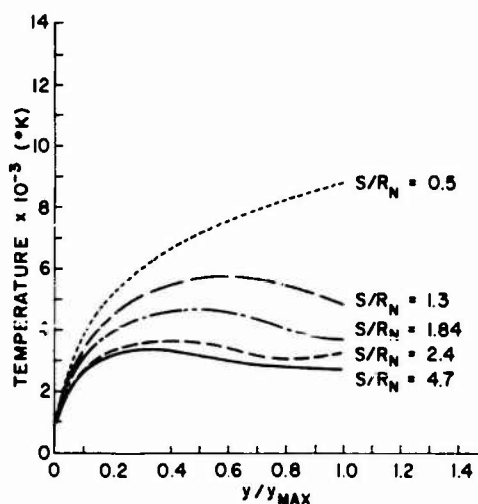


Figure 48. Temperature Profiles at Various Vehicle Locations for 240 kft and  $V_{\infty} = 17,500$  fps

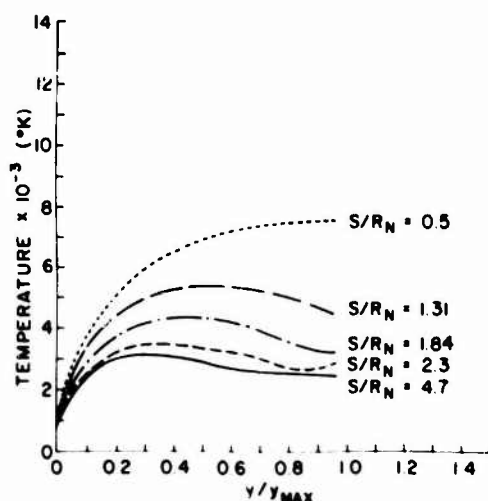


Figure 49. Temperature Profiles at Various Vehicle Locations for 240 kft and  $V_{\infty} = 16,500$  fps

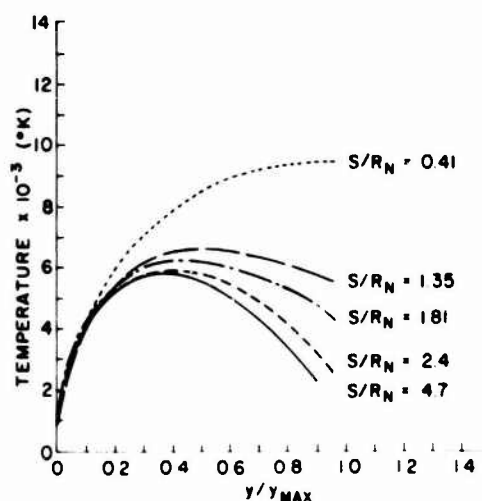


Figure 50. Temperature Profiles at Various Vehicle Locations for 270 kft and  $V_{\infty} = 17,500$  fps

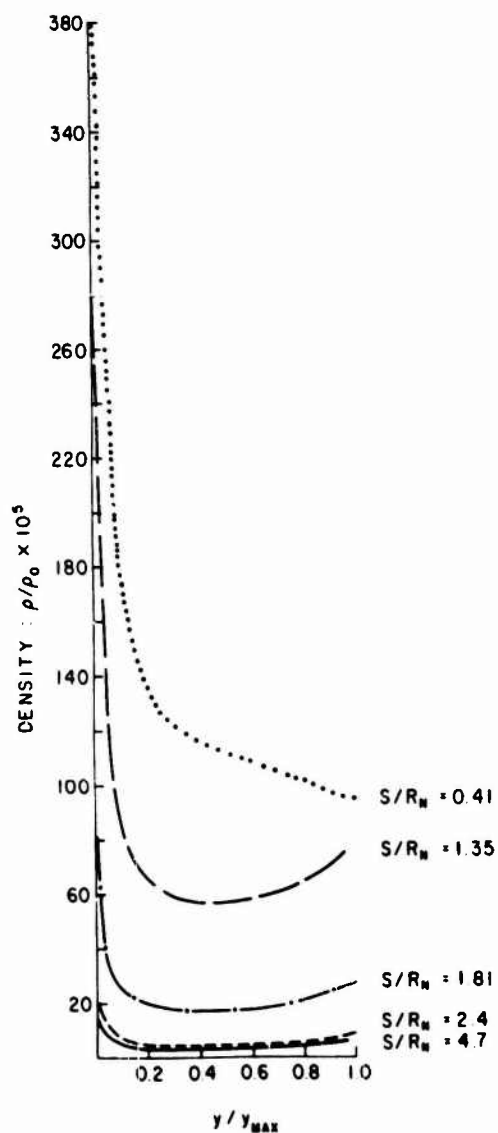


Figure 51. Density Profiles at Various Vehicle Locations for 220 kft and  $V_\infty = 17,500$  fps

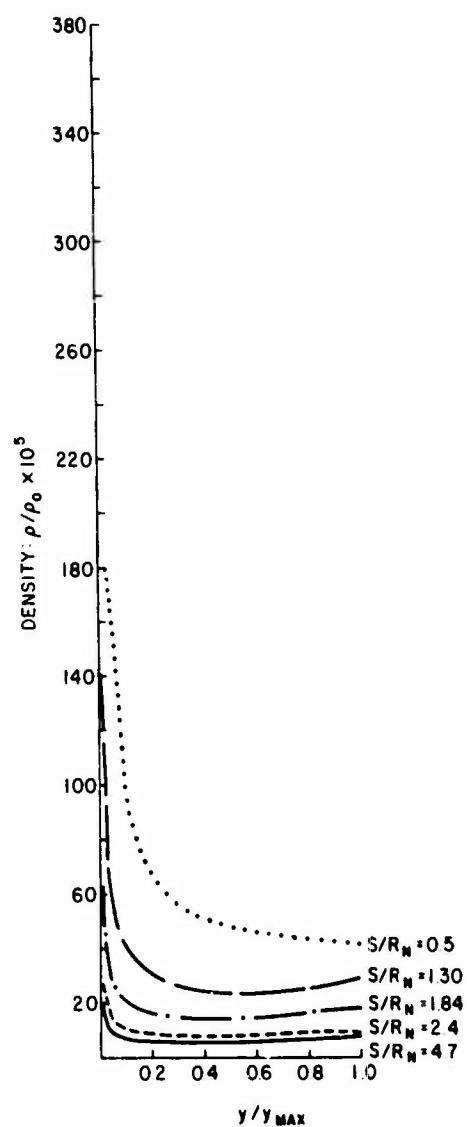


Figure 52. Density Profiles at Various Vehicle Locations for 240 kft and  $V_\infty = 17,500$  fps

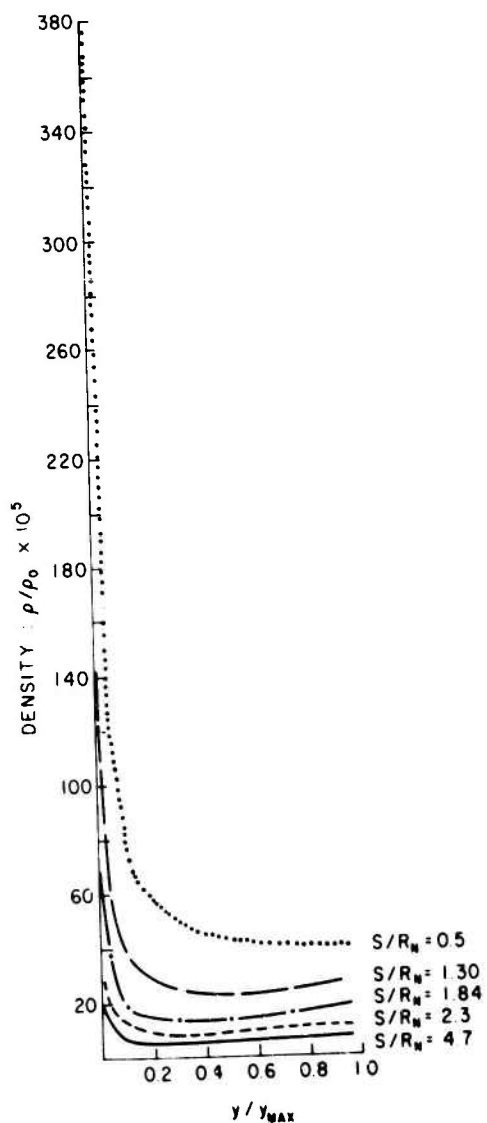


Figure 53. Density Profiles at Various Vehicle Locations for 240 kft and  $V_\infty = 16,500$  fps

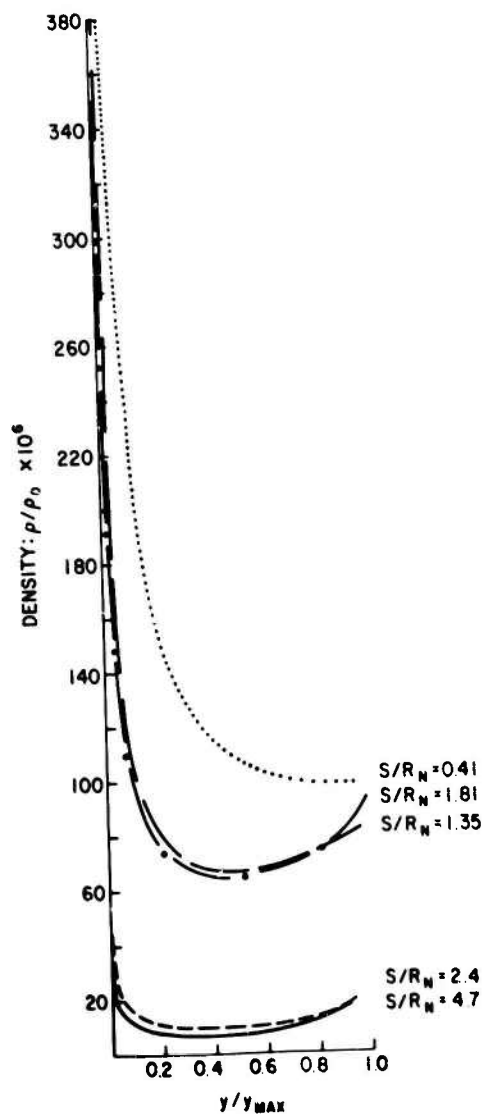


Figure 54. Density Profiles at Various Vehicle Locations for 270 kft and  $V_\infty = 17,500$  fps

likewise not vary significantly. Then with the nose region having a dominant effect on the flow condition, it should be possible to characterize the vibrational equilibrium flow property profiles around the vehicle in terms of a ratio based on known profile values in the stagnation region. Results from such an approach would be reasonable and can be demonstrated by considering the results at a typical condition. This is shown in Figure 55. The electron density profiles at 240 kft for the two cases:  $V_\infty = 16,500$  fps and  $V_\infty = 17,500$  fps have the constant relation that:

$$3.0 \times (n_e)_{16.5} \approx (n_e)_{17.5}$$

This represents a justification for the assumption since the ratio has the same value in the stagnation region, Figure 20. Thus this can be considered a reasonable approach to estimating results at slightly different initial conditions. The constancy of the ratio at all locations around the vehicle also tends to justify the use of the 240 kft results for the body station profiles at  $V_\infty = 16,500$  fps to represent equivalent results for  $V_\infty = 17,500$  fps at the nominal altitude of 246 kft based on the

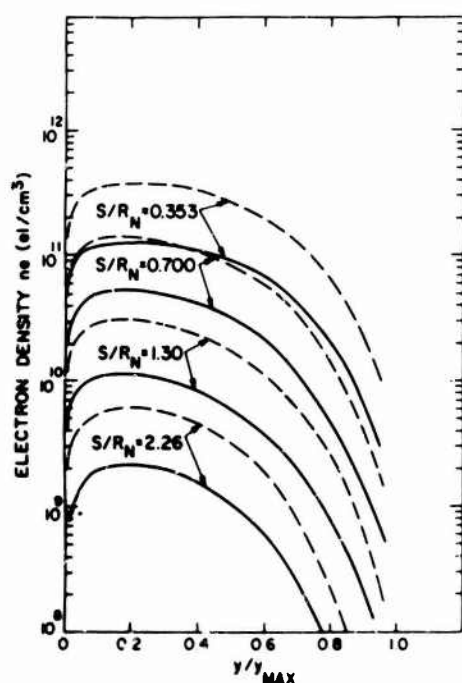


Figure 55. Comparison of the Electron Density Profiles Around the Vehicle at 240 kft for (—)  $V_\infty = 17,500$  fps and (---)  $V_\infty = 16,500$  fps

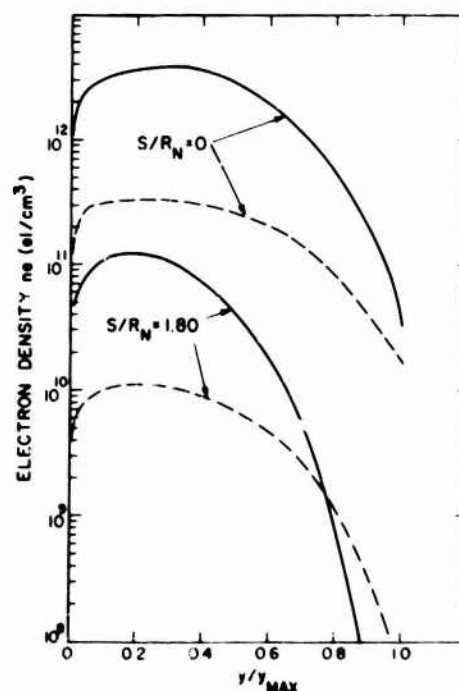


Figure 56. Comparison of the Stagnation ( $S/R_N = 0$ ) and Shoulder Region ( $S/R_N = 1.8$ ) Electron Density Profiles for  $V_\infty = 17,500$  fps at (—) 220 kft and (---) 240 kft

comparison of stagnation results as shown in Figure 24. These variations allow the extension of a limited set of results to cover a wider range of conditions than were specifically calculated.

One further approach to extending these results was considered. Based on similar arguments of nose region dominance, there was a faint hope that the distributions around the vehicle at interpolated altitudes could have been determined from the values in the stagnation region. The ratio of electron densities at various locations on the profiles at  $S/R_N = 0$  and  $S/R_N = 1.8$  were compared at 220 kft and 240 kft in Figure 56. The respective ratios did not show any consistency. The failure of this approach is due to a number of reasons, including the fact that the profiles undergo a significant change in shape with decreasing altitude and differences in the matching problem for the two solutions at various altitudes.

### 5.3.5 LOW ALTITUDE THEORY

In order to produce a more complete picture of the flow properties for Trailblazer II, some additional calculations were performed at lower altitudes, although in general the instrumentation was either saturated or experiencing black-out conditions in this regime. Since this was the case, however, the properties were not determined in the detail or accuracy of the higher altitude cases where changing values produced significant variations in the experimental behavior. The viscous and inviscid regions are now quite distinct, and the boundary layer has

become compressed into a small region near the surface. Their relative magnitudes for some typical conditions at  $S/R_N = 1.2$  can be seen in Figure 57. The curves indicate the variation of these flow dimensions as a function of the freestream velocity for altitudes of 160 kft and 180 kft. Based on the resulting ratio of boundary-to-shock thickness some interaction might still be expected at the higher end of the altitude range, but as a first approach this was neglected. An equilibrium inviscid flow was calculated along the lines of Evans et al (1970). This was then modified near the surface by using similar boundary layer values to produce a single overall distribution profile for the entire shock layer. This degree of accuracy

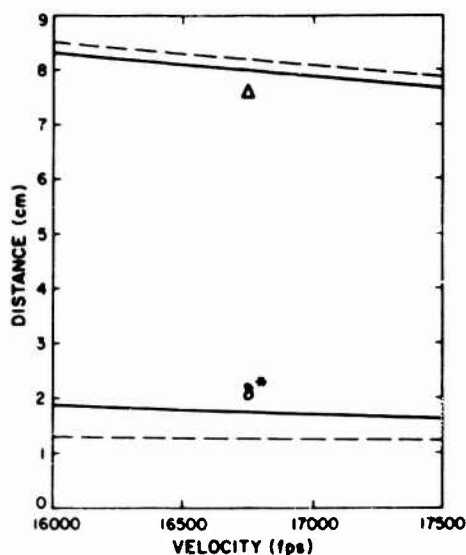


Figure 57. The Effect of Velocity on Shock ( $\Delta$ ) and Boundary Layer ( $\delta^*$ ) Thicknesses at (—) 180 kft and (---) 160 kft

seemed to be all that was called for in the circumstances, and will be discussed in a later section.

Figure 58 shows the stagnation streamline electron density distributions at 160 kft and 180 kft as a function of velocity. In all cases, the curves are similar and quite smooth. Once the shoulder has been reached the slope becomes small, and the conical type behavior takes over. For this reason, the properties in this region are considered to be represented by the typical profiles shown in Figure 59 for  $S/R_N = 1.8$ . The velocity dependence is shown, and it is clear that for all conditions the curves are again similar in shape. This location was selected since it corresponds to a reasonable point for both antenna and probe comparisons in the shoulder region. The greatest differences in the profiles occurred at the peak values, and they were within half an order of magnitude. Under the circumstances of the present flights, it was assumed to be unlikely that significant error would be introduced by this approach of representative cases. Since most of the flight data away from the nose region came from the third flight, a velocity history which would be compatible with it was used in calculating the overall low altitude electron density profiles for comparison with experiment. The selected cases are outlined in Table 6. The results of these calculations are shown in Figure 60. The equilibrium results are all similar, but the frozen profile is significantly higher in peak value and has an atypical fall-off toward the shock.

The original concept was that in the comparison with the flight data the 177-kft equilibrium result would give good agreement, while the frozen case would represent a large overestimate. In the actual case, however, it was found that although the latter aspect was satisfied, the former case produced results that underestimated the situation by a considerable margin. Thus for this altitude and for the 260-kft case, a further refinement had to be considered.

Ball et al (1965) reported some results which had the correct flight velocity for these two cases. Their approach involved an iterative procedure that accounted for boundary layer swallowing, contained a more sophisticated viscous-inviscid matching process, and allowed finite rate chemistry along streamlines. The profiles for the two altitude conditions are shown in Figure 61. The curves are closer to the shape of the frozen case at 177 kft and the corresponding results are between that curve and the equilibrium values.

With the completion of the theoretical description of the flow in the expansion region as far as was required for Trailblazer II purposes at this stage, the next step will be to compare these calculations with the variety of data from the three flights.

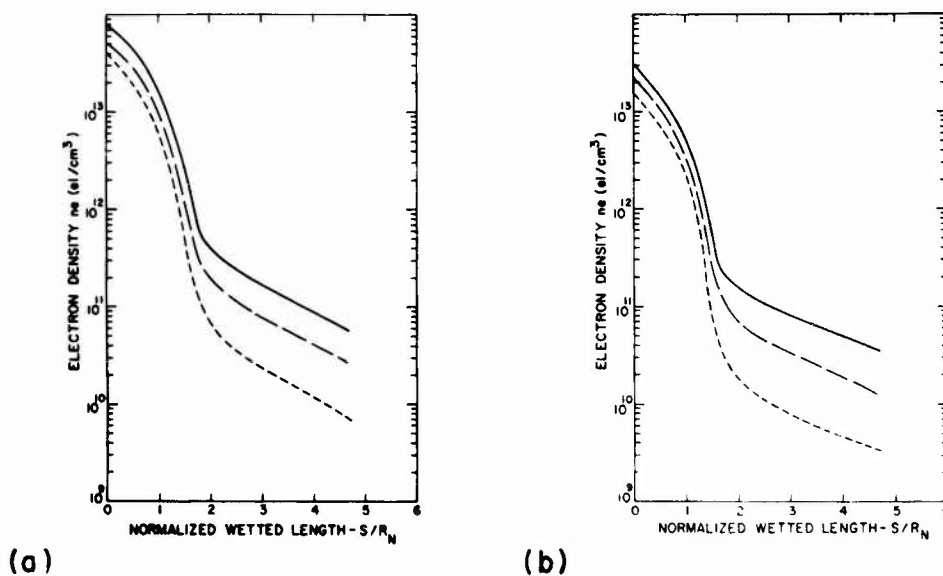


Figure 58. Stagnation Streamline Equilibrium Electron Density: (a) 160 kft, and (b) 180 kft. (—)  $V_\infty = 17,500$  fps, (---)  $V_\infty = 16,500$  fps, and (- - - -)  $V_\infty = 16,000$  fps

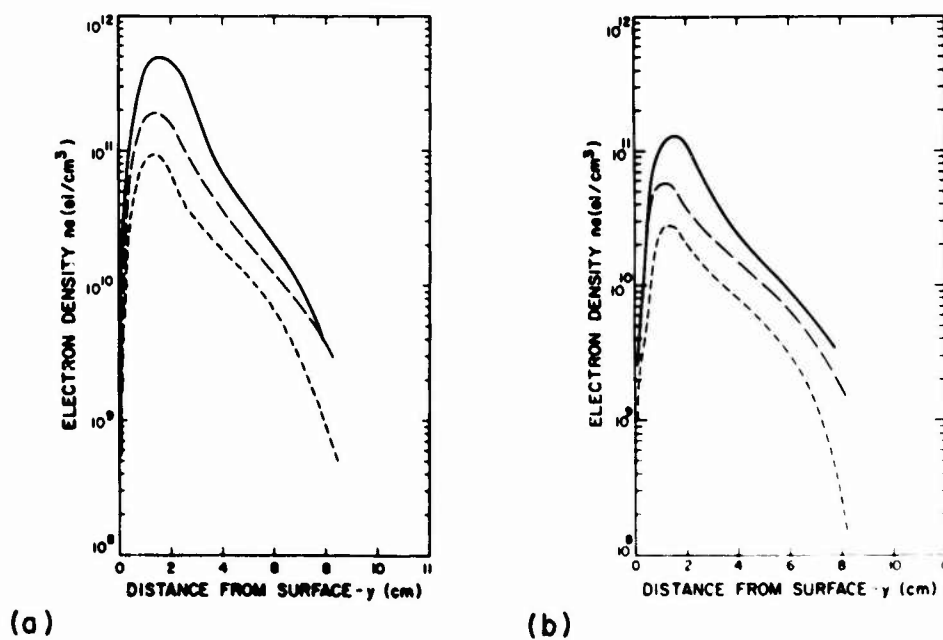


Figure 59. Effect of Velocity on Electron Density Profiles at  $S/R_N = 1.8$ : (a) 160 kft, and (b) 180 kft, (—)  $V_\infty = 17,600$  fps, (---)  $V_\infty = 16,500$  fps, and (- - - -)  $V_\infty = 16,000$  fps

Table 6. Description of the Selected Low Altitude Conditions

Altitude (kft)	Velocity (kft/sec)	Comment
200	17.5	Equilibrium; $S/R_N = 1.2$
177	17.85	(OSU) Equilibrium; (OSU) Frozen $S/R_N = 1.57$
150	17.0	Equilibrium; $S/R_N = 1.2$
130	16.5	Equilibrium; $S/R_N = 1.2$
100	14.6	Equilibrium; $S/R_N = 1.2$

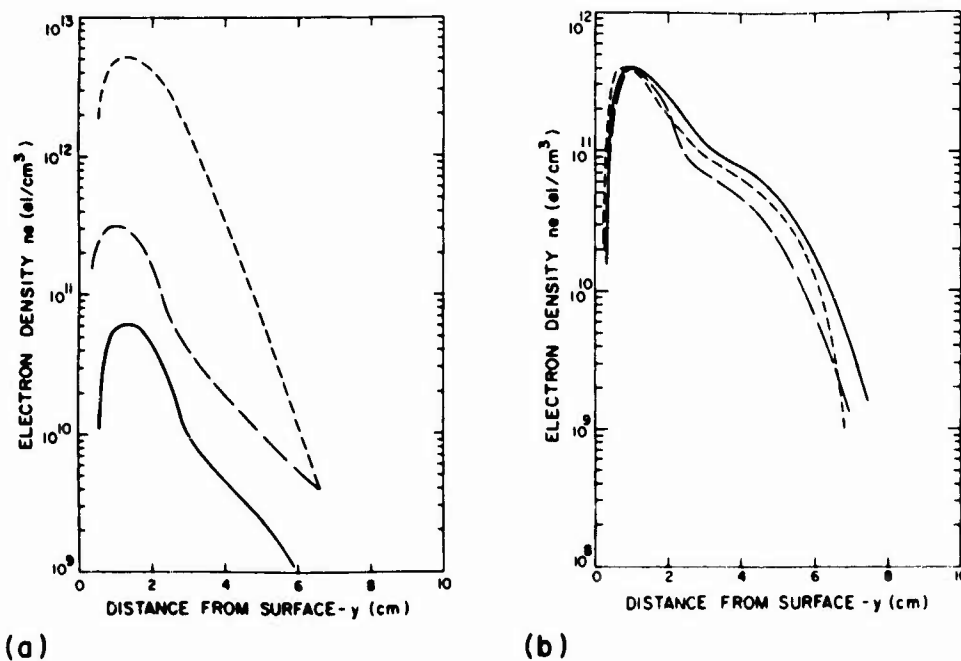


Figure 60. Electron Density Profiles at Shoulder. (a) (—) 200 kft; (---) 177 kft, OSU equilibrium; (- - - -) 177 kft, OSU frozen; and (b) (—) 150 kft; (---) 130 kft; (- - - -) 100 kft



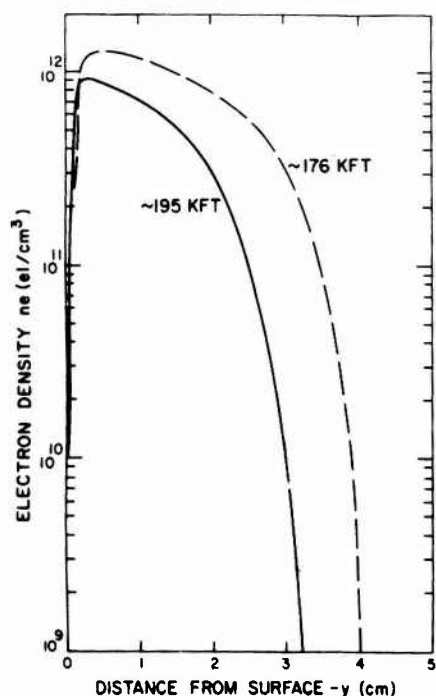


Figure 61. Nonequilibrium Electron Density Profiles at the Shoulder: (—) ~ 195 kft, and (---) ~ 176 kft

### 5.3.6 PROBE DATA COMPARISONS

The purpose of the various theoretical calculations over the entire altitude range of reentry was to establish the ability of these techniques to predict the performance of the microwave devices that composed the experimental packages of the three flights. This becomes less important once the plasma becomes intense enough to saturate sensors and black out signal transmission, but the buildup of these effects is significant. Since the present section is concerned with the expansion flow, the reliability of the theories used should deteriorate beyond the point on the vehicle where an axisymmetric cross section still exists for the particular angle of attack of each flight.

The two types of vehicle instrumentation which are available for comparison are surface sensors and microwave transmitters.

Thus the same type of evidence around the vehicle is available for discussion as in the nose region. The data represent results from all of the flights. See Figure 3 for a summary of the various experimental devices.

On the first two flights, some electroacoustic probes were flown. These had only limited results since the presence of spin and angle of attack allowed only one resonance to be observed. (For more details see Poirier et al, 1967). The data that were obtained were in agreement with the electrostatic probe results. On the third flight there was a microwave stripline, but the results of this have not as yet been fully analyzed. The instrumentation of that flight also contained a dual level conductivity probe located at the shoulder. [ See Aisenberg and Chang (1971) for an analysis of the probe and its operation. ] Theoretical calculations of the plasma conductivity indicate that below an altitude of 270 kft, levels on the order of several mho/meter exist quite close to the vehicle surface, well within the probe sheath heights of 0.25 and 1.0 in. See, for instance, Figure 35 through Figure 38. During the flight, however, the only response that could even possibly be considered as other than noise registered near the end of the reentry period at around 130 kft. The highest reading that could be assigned to that response was at least an order

of magnitude below both the predicted values and electrostatic probe correlations. Inasmuch as this occurred at a point where theory predicts that the conductivity level should have been decreasing from the levels of the previous altitudes and given the minimal nature of the reading, there remains a strong question as to whether the probes were functioning in the proper manner during reentry.

The electrostatic probes at various positions were analyzed in similar fashion as in the nose region, except that the angle of attack effect had to be included. The first approximation was to assign positions for the windward and leeward values which corresponded to the distance from the shifted stagnation point location. This should be a reasonable approximation as long as the position is within the region of symmetry. Further downstream the approach is invalid as a result of the three-dimensional flow pattern.

Inasmuch as the stagnation profiles assuming vibrational nonequilibrium proved to be in better agreement with the data, an attempt was made to account for this effect around the vehicle in analyzing the probe data. The existing vibrational equilibrium profiles at a given altitude were modified by a factor corresponding to the ratio of the two results in the stagnation region. This is an upper bound type of approach since the reaction time increase should reduce the degree of vibrational nonequilibrium present in the flow. Thus the further back on the vehicle the probe was located, the more the approximated nonequilibrium profile should overestimate the actual condition.

Figure 62 shows the electron density altitude history for the variable bias probe at the assigned windward position  $S/R_N = 0.3$ . The theoretical vibrational equilibrium values follow the trend of the results closely, and the approximate nonequilibrium vibration values are still in an almost perfect agreement. The variable bias corresponds to three different probe sheath thicknesses and hence offers the opportunity for comparison with the overall theoretical profile at a probe location. The relationship between the theoretical and probe profiles at two altitudes can be seen in Figure 63 for both windward and leeward orientations of this probe. The ability of the probes to indicate the variation in electron density across the sheath is quite good for all cases. The worst result is an overestimation by less than a factor of 1.5 for the leeward side at 240 kft. For a probe located on the vehicle at  $S/R_N = 2.6$ , however, the results for both windward and leeward conditions which are shown in Figure 64 are almost an order of magnitude greater than the vibrational equilibrium predictions. This would tend to confirm the breakdown of the zero angle of attack calculation for the rear of the vehicle. In Figure 65 the results for the three probes including windward and leeward assigned locations are indicated at an altitude of 240 kft. The theoretical results are also presented, including the estimated values for vibrational nonequilibrium. Near the front of the vehicle, where there is still symmetry and the degree of vibrational

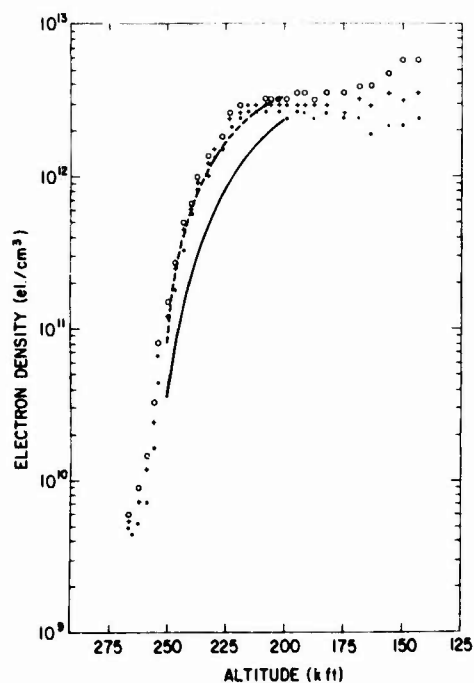


Figure 62. Electrostatic Probe Electron Density at a Windward Position of  $S/R_N = 0.3$ , Compared to Theory. The three bias settings are shown: ( $\bullet$ ) -5V; ( $+$ ) -15V; ( $\circ$ ) -30V; and the theoretical models with (—) for vibrational equilibrium and (---) for vibrational nonequilibrium

Figure 63. Variable Bias Electrostatic Probe Data at 220 kft and 240 kft for Windward ( $S/R_N = 0.3$ ) ( $+$  —  $+$ ) and Leeward ( $S/R_N = 0.65$ ) ( $+$  ---  $+$ ) Compared to Theory for Windward (—) and Leeward (---)

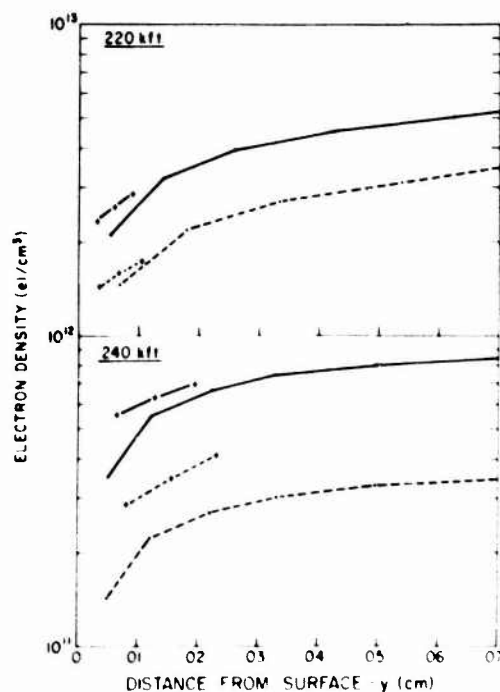


Figure 64. Variable Bias Electrostatic Probe Electron Density for a Windward Position ( $S/R_N = 2.4$ ): ( $\bullet$ ) -5V; ( $+$ ) -15V; and ( $\circ$ ) -30V. There is a microwave correlation ( $\square$ ) and theory shown as ( $\oplus$ )

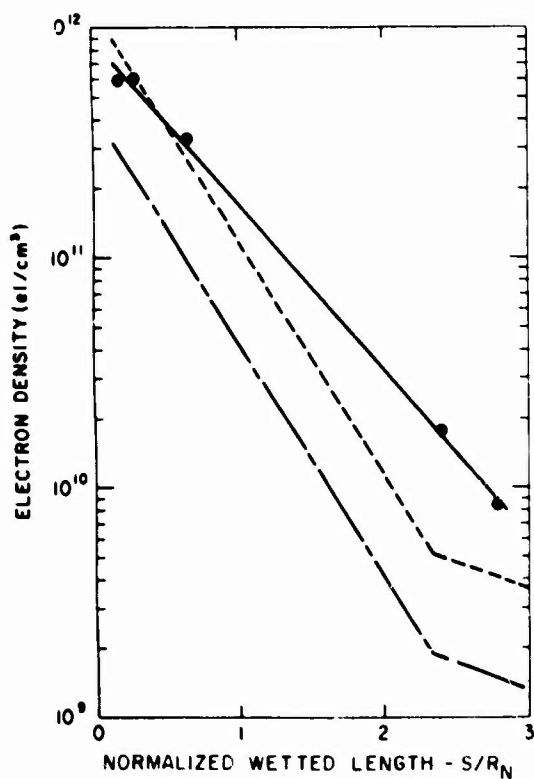
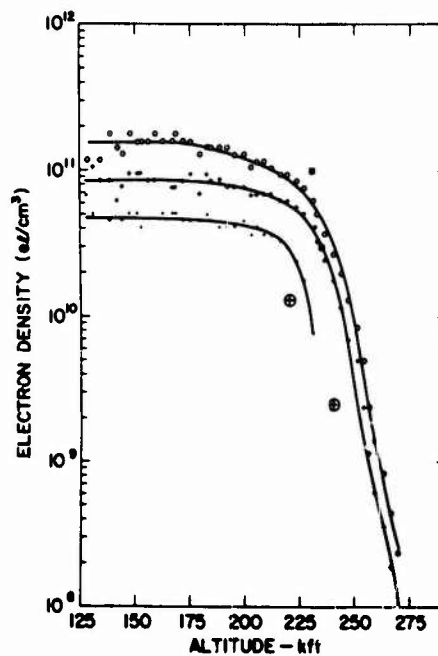


Figure 65. The Variation Around the Body of the Electron Density Near the Surface Based on Data ( $\oplus$ ) and a Straight Line fit (—). The theoretical values for vibrational equilibrium (---) are shown along with a nonequilibrium estimate (.....) using a correction factor

nonequilibrium should be relatively unchanged, the agreement is still fair. However, taking into consideration that the approximation should represent an upper bound the agreement rapidly deteriorates. Indeed, beyond  $S/R_N \approx 2$  the assignment of windward and leeward positions to interpret probe results has become so invalid that the transition from spherical to conical flow results does not appear in the curve representing the electrostatic probe data. The need for three-dimensional flow calculation is clear.

The probe results were not extended to lower altitudes for a number of reasons. First, as the density rises the possibility of electron scattering outside the probe sheath becomes important and the model does not include this. Secondly, with increasing electron density the sheath thickness becomes quite small so measurements on the fall off portion of the profile near the surface would no longer serve to indicate external electron density levels. In addition, the nearness to the surface introduces a stronger dependence on wall conditions and the effects of flow behavior near a surface were not extensively studied in any of theoretical results employed.

### 5.3.7 SHOULDER ANTENNA

In addition to the various probe comparisons, the theoretical flow properties around the vehicle can be evaluated from the observed antenna performance characteristics during the reentry. Numerous studies of the antenna results are being carried out including some quite sophisticated analyses of antenna patterns and coupling in the presence of the external ionized layer. Until these results are available, however, some more basic approaches on a quite simplified model can be offered for comparison. Estimates of the plane wave attenuation and reflection were made along the lines indicated by Russo (1963). The variation of the attenuation constant along the normal to the antenna is first determined. An integration is then carried out over this distribution to obtain the signal loss in the plasma medium due to attenuation.

$$(S.L.)_A = 8.686 \int_0^{y_{MAX}} \alpha \, dy$$

where

$$(\alpha/k) = \left( \frac{|K| - K_r}{2} \right)^{1/2} \quad |K| = (K_r^2 + K_i^2)^{1/2}$$

and

$$(\beta/k) = \left( \frac{|K| + K_r}{2} \right)^{1/2} \quad k = \omega/c$$

For the reflection, an equivalent slab thickness associated with the peak  $\alpha$  value is then determined:

$$d_E = \left( \int_0^{y_{MAX}} \alpha dy \right) / \alpha_{MAX} .$$

The peak attenuation constant, its corresponding phase constant, and the effective thickness then serve to specify the reflection loss:

$$(S.L.)_R = 10 \log_{10} \left( \frac{1}{1-R} \right)$$

where

$$R = \frac{R_{12} [(1 - e^{-2\alpha d_E})^2 + 4 e^{-2\alpha d_E} \sin^2 \beta d_E]}{(1 - R_{12} e^{-2\alpha d_E})^2 + 4 R_{12} e^{-2\alpha d_E} \sin^2 (\delta_{12} + \beta d_E)}$$

with

$$\delta_{12} = \tan^{-1} \left( \frac{2k\alpha}{k^2 - \beta^2 - \alpha^2} \right) \quad \text{and} \quad R_{12} = \left( \frac{(k - \beta)^2 + \alpha^2}{(k + \beta)^2 + \alpha^2} \right) .$$

The profiles at the shoulder over the entire altitude range of reentry were used as inputs to these calculations. The overall results for the flight history are summarized in Table 7. Figure 66 shows the altitude variation in signal attenuation for the test antenna based on received signal peak values at the ground station. The theoretical predictions are in quite good agreement with the profile, being within 5 kft over the entire range for which flight data is available. This is somewhat unexpected, considering the many approximations involved. The theory for the low altitude range indicates that as the vehicle slows down, there should be some recovery in the signal loss. There was no indication of this in the available flight data, but it should be pointed out that these measurements depend on the reception of the signal by the ground stations. Once the signal becomes effectively blacked out, the radars can no longer maintain a continuous track. Thus if at some further point in the trajectory the plasma attenuation did decrease, it is quite possible that the ground radars would be unable to detect it.

In contrast the data for the power reflection coefficient are available down to 130 kft although the quality of the data is not uniform below 170 kft. Values corresponding to windward and leeward orientations of the antenna are shown in

Table 7. S-Band Shoulder Antenna Transmission Properties

Altitude (kft)	Velocity (fps)	R	SL <sub>R</sub> (db)	SL <sub>A</sub> (db)	SL <sub>T</sub> (db)
240	17,500	0.0003	0.001	0.014	0.015
235	17,500	0.001	0.006	0.032	0.038
230	17,500	0.007	0.032	0.085	0.117
225	17,500	0.166	0.789	1.83	2.62
220	17,500	0.690	5.1	12.22	17.32
215	17,500	0.921	11.0	16.43	27.43
195	17,500	0.981	17.2	26.18	43.38
177	17,500	0.968	14.95	41.17	56.12
150	17,000	0.861	8.58	18.59	27.17
130	16,500	0.783	6.6	22.4	29.0
100	14,600	0.315	1.64	13.36	15.0

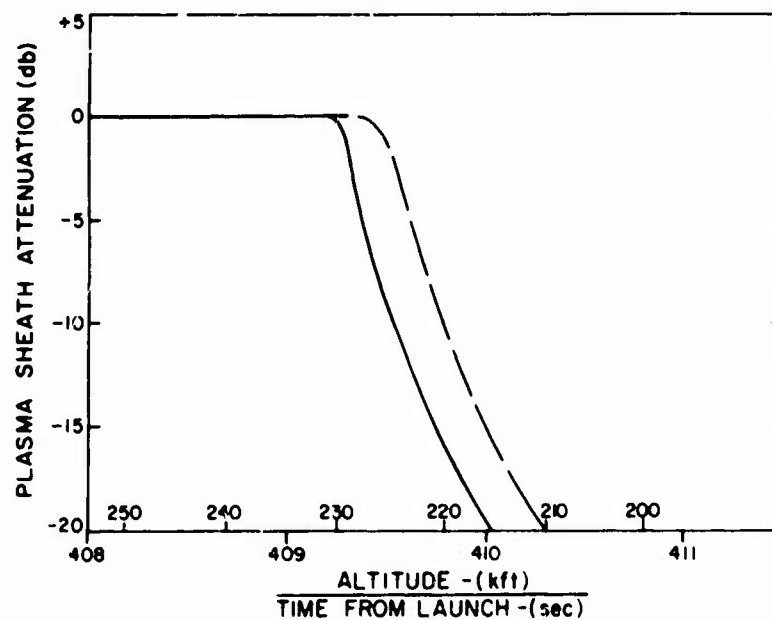


Figure 66. Third Flight Shoulder Antenna Signal Attenuation: (—) flight data, and (---) theory

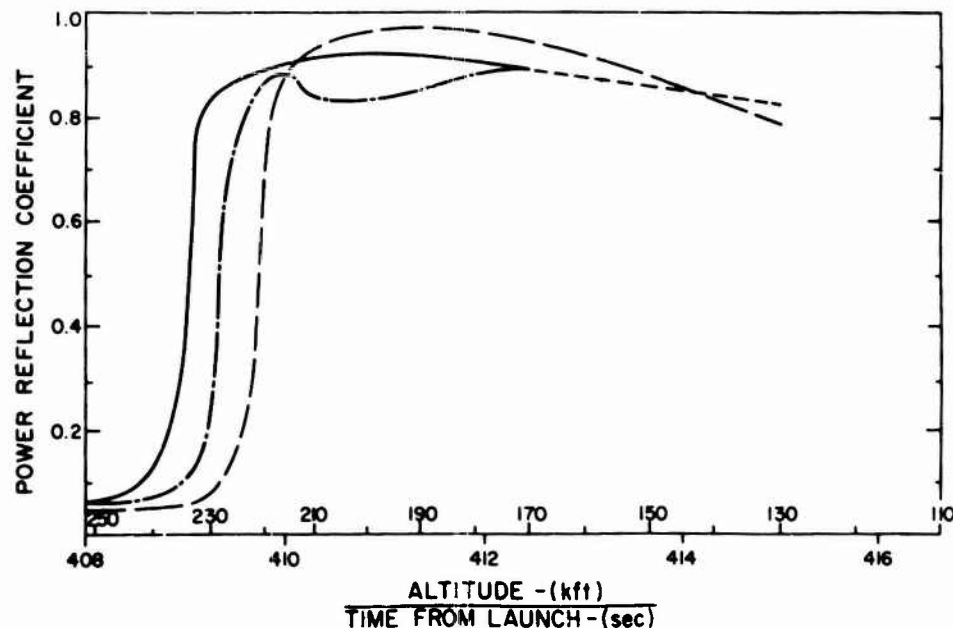


Figure 67. Third Flight Shoulder Antenna Power Reflection Coefficient: (—) theory, flight (---) windward, and (- - -) leeward; (---) region where signal was intermittent

Figure 67, along with the mean theoretical predictions. As in the case of the attenuation, the abrupt rise in value occurred at slightly lower altitude than was the case for the stagnation antenna, as was expected. The theoretical results again indicate a slight underestimation of the plasma but the slope of the profile is the same, and the values correspond to within 10 kft. The overall trend once the peak reflection has been reached is also in excellent agreement, and the tendency for plasma effects to diminish at the lower altitudes is also confirmed. These data points are available since they are based on vehicle measurements rather than ground ones. As long as the telemetry signal is being received, the reflection can be determined.

#### 5.3.8 SUMMARY OF EXPANSION REGION RESULTS

The overall agreement between predictions and actual test results is encouraging. If the vibrational nonequilibrium effects had been estimated at the higher altitudes in a similar fashion to the probe analysis, the predicted onset of the rise in plasma effects would have been even closer. Thus, despite the fact that some angle of attack effects should have come into play, the theory still is a satisfactory predictor.



## 6. SUMMARY AND CONCLUSIONS

This report has described the aerodynamic performance of the first three AFCRL Trailblazer II Rocket flights and has compared predictions of the reentry flow field properties with the experimental results. The following observations outline this material:

- (1) Vehicle performance, orientation, and several additional parameters necessary for interpretation of the flight data are included.
- (2) Details of various models used to describe the properties of the ionized medium surrounding the flight vehicle during reentry are discussed. The results of these calculations are presented for various altitudes both in the stagnation region and at locations in the expanded flow around the vehicle.
- (3) Some estimates of effects due to changing reentry velocity and the influence of the vehicle spin and the angle-of-attack-induced flow asymmetry are discussed in relation to predictions using the axisymmetric assumption of the models.
- (4) In general most of the results were based on the antennas and the electrostatic probes, while other data were either uncertain, too limited, or as yet unanalyzed.
- (5) The antenna results in the stagnation region were in quite good agreement with the completely viscous vibrational nonequilibrium model, while even the vibrational equilibrium results indicated the correct trend although not at the same altitude.
- (6) In the stagnation region the same overall agreement was found for the probe results, although the problem at 270 kft altitude, where the electron density predictions are all orders of magnitude lower than the levels given by probe analysis, has not been resolved.
- (7) In the expansion region, probe data were compared only at high altitudes where probe sheath thicknesses were reasonable.
- (8) The probe data around the vehicle was in agreement with theory only on the nose cap. Three-dimensional effects invalidated the comparison further back.
- (9) The vibrational equilibrium model was in reasonable agreement with signal attenuation results for the shoulder antenna as far as the data were available. Inclusion of a nonequilibrium factor, as in the probe case, should introduce even better conformity.
- (10) The reflection data from the shoulder antenna were obtained over most of the flight regime. The predicted history, based on the combined results of the various altitude models, was quite close to the actual profile.
- (11) The decrease in plasma effects as the reentry velocity lessened could be seen in the flight data and was also present in the theoretical results.

(12) The high altitude predictions for the power reflection coefficient could also be improved by including a factor for vibrational nonequilibrium.

(13) The failure of predictions once the flow has become distinctly three-dimensional points to the need for including this factor in theoretical estimates of properties back on the vehicle.

The general conclusion, however, is that sufficient agreement with a number of flight experiments under various plasma conditions can be obtained despite the generally approximate nature of the models.

## Acknowledgments

The author wishes to acknowledge the many individuals at AFCRL who contributed to this report on the Trailblazer II flights. The overall flight program is under the supervision of Walter Rotman. On a number of points, discussions with J. L. Poirier and D. Hayes proved valuable. The final draft received a thoughtful reading by R. Newburgh and his criticisms are appreciated as are those of R. Mailloux. The many comments made by H. Lew of General Electric, Valley Forge, Pennsylvania, on details of his theoretical calculations were especially helpful. Finally, all those who are a part of the Trailblazer II program must be mentioned and this of course includes Ms. A. Zouvelos who had to cope with deciphering the manuscript.

## References

- Aisenberg, S. and Chang, K.W. (1971) Chemical Additives and Diagnostics for High Temperature Air Plasmas, AF CRL-72-0354, Final Rpt Contract No. F19628-71-C-0077.
- Allen, H.J. (1957) Motion of a Ballistic Missile Angularly Misaligned With the Flight Path upon Entering the Atmosphere and Its Effect Upon Aerodynamic Heating, Aerodynamic Loads and Miss Distance, NACA Technical Note TN 4048.
- Ball, W.H., Webb, H.G., Jr., and Lyon, F.J. (1965) Flow Field Predictions and Analysis, Study for Project RAM B3, Space and Information Systems Division Final Rpt No. SID-65-1113, Rpt No. NASA-CR-66106 Contract NAS 1-4743, North American Aviation, Inc.
- Caldecott, R., Bohley, P., and Nerem, R. (1967) Reentry Communications: Antenna Impedance and Radar Reflection Recorded During the Reentry of a Trailblazer Rocket Vehicle on 14 Feb 66, Electroscience Laboratory Rpt No. 2146-7 Contract AF33(615)-3466, Ohio State University Research Foundation.
- Caldecott, R., and Bohley, P. (1968) Radio Frequency Noise During Reentry: Measurements Made at 2235 Mc/s During the Reentry of a Trailblazer Rocket Vehicle, Electroscience Laboratory Rpt No. 2151-7 Contract AF33(615)-3258, Ohio State University Research Foundation.
- Curtis, J., Burke, A., and Hayman, R. (1963) An Analytical and Experimental Study of the Ionized Flow Field About a Hemisphere Cylinder and Its Effect on the Radiation Pattern of a Slot Antenna, Final Rpt No. AF CRL-63-339, Contract AF19(604)-8494, Cornell Aeronautical Laboratory.
- Evans, J.S., Schexnayder, C.J., and Huber, P.W. (1970) Computation of ionization in re-entry flowfields, AIAA J. 8(No. 6):1082-1089.
- Fay, J.A. and Riddell, F.R. (1958) Theory of stagnation point heat transfer in dissociated air, J. Aero/Space Sci. 25(No. 2):73-85.
- Hayes, D.T. (1972) Electrostatic Probe Measurements of Flow Field Characteristics of a Blunt Body Reentry Vehicle, AIAA Paper 72-694 5th Fluid and Plasma Dynamics Conference, Boston, Mass.

- Hayes, D.T., Herskovitz, S.B., Lennon, J.R. and Poirier, J.L. (1972) Preliminary Report on the Trailblazer II Chemical Alleviation Flight of 28 July 1972, AFCRL-72-0640.
- Leon, H.I. (1958) Angle of attack convergence of a spinning missile descending through the atmosphere, J. Aeron. Sci. 25(No. 8):480-484.
- Lew, H.F. (1970) Shock Layer Ionization at High Altitudes, AFCRL-70-0702, Final Report on Contract F19628-69-C-0112, GE 70-SD782, The General Electric Co., Valley Forge, Pennsylvania.
- Nerem, R. (1962) Stagnation Region Plasma Properties Including Some Non-uniform Effects, Aerodynamics Laboratory Rpt No. 1021-25 Contract No. AF33(616)-6782, Ohio State University Research Foundation.
- Poirier, J.L., Rotman, W., Hayes, D.T. and Lennon, J.F. (1969) Effects of the Reentry Plasma Sheath on Microwave Antenna Performance: Trailblazer II Rocket Results of 18 June 1967, AFCRL-69-0354.
- Rotman, W. (1972) Microwave Measurements of Flow Field Characteristics at the Stagnation Point of a Blunt Reentry Body, AIAA J. Preprint, AIAA 5th Fluid and Plasma Dynamics Conference, Boston, Mass.
- Russo, A.J. (1963) Estimates of Attenuation and Reflection of Telemetry Signals by Ionized Flow Fields Surrounding Typical Reentry Bodies, NASA Technical Note TN D-1778.
- Scharfman, W.E. and Bredfeldt, H.R., (1967) Experimental Studies of Electrostatic Probes for the Reentry Measurements Program-Phase B, Subcontract 611603 under Prime Contract 30-0690AMC-333(Y), SRI Project 6138, Stanford Res. Inst. Menlo Park, California.

Unclassified

Security Classification

DOCUMENT CONTROL DATA - R&D		
(Security classification of title, body of abstract and indexing annotation must be entered when the overall report is classified)		
1. ORIGINATING ACTIVITY (Corporate author) Air Force Cambridge Research Laboratories (LZ) L. G. Hanscom Field Bedford, Massachusetts 01730		2a. REPORT SECURITY CLASSIFICATION Unclassified 2b. GROUP
3. REPORT TITLE TRAILBLAZER II ROCKET TESTS ON THE REENTRY PLASMA SHEATH: VEHICLE PERFORMANCE AND PLASMA PREDICTIONS (Flights No. 1-3)		
4. DESCRIPTIVE NOTES (Type of report and inclusive dates) Scientific. Interim.		
5. AUTHOR(S) (First name, middle initial, last name) John F. Lennon		
6. REPORT DATE 16 May 1973	7a. TOTAL NO. OF PAGES 84	7b. NO. OF REFS 17
8a. CONTRACT OR GRANT NO.  b. PROJECT, TASK, WORK UNIT NOS. 46420201 c. DOD ELEMENT 62101F d. DOD SUBELEMENT 681000		9a. ORIGINATOR'S REPORT NUMBER(S) AFCRL-TR-73-0317  9b. OTHER REPORT NO(S) (Any other numbers that may be assigned this report) PSRP No. 549
10. DISTRIBUTION STATEMENT Distribution limited to U.S. Government agencies only; Test and Evaluation, 18 April 1973. Other requests for this document must be referred to AFCRL, LZ, L. G. Hanscom Field, Bedford, Massachusetts 01730		
11. SUPPLEMENTARY NOTES  TECH, OTHER ↓		12. SPONSORING MILITARY ACTIVITY Air Force Cambridge Research Laboratories (LZ) L. G. Hanscom Field Bedford, Massachusetts 01730
13. ABSTRACT The properties of the reentry plasma sheath are being studied by AFCRL in a series of Trailblazer II rocket flights. This program is divided into two phases. The first phase has been concerned with the structure of the ionized layer that forms around the test vehicles during reentry and in particular its effect on electromagnetic signals, while the second phase is concerned with enhancing microwave transmitter performance under such conditions by introducing chemicals into the flow to reduce the free electron concentrations.  This report surveys some aspects of the first phase which consisted of three flights. The first part of the report describes the flight performance of the vehicles including trajectory, velocity history, aerodynamic heating, spin-and-precession, and overall orientation of each payload during its reentry, while the second part presents a theoretical description of the high temperature shock layer for the various flight conditions. Since the purpose of the calculations was to obtain predictions of experimental performance, a number of different models were used. The resulting flow properties are presented in some detail; in particular, the various electron density distributions are shown both in the nose region and around the vehicle. These results are analyzed and then compared with the extensive experimental data.  On the conical afterbody where three-dimensional effects due to vehicle angle of attack become important, the observed conditions could not be completely represented by the theoretical models—all of which assumed the flow to be axisymmetric. The general conclusion, however, is that the theoretical properties satisfactorily predict the actual test performance for a wide range of situations.		

DD FORM 1473  
1 NOV 65

Unclassified  
Security Classification

